



Single exposure reflectance measurements by means
of multiple angles-of-incidence with conventional and
unconventional polarization states of light

(Final version. Changes suggested by advisors are included)



Maestría en Ciencias (Óptica)
(Master of Science –Optics–)

Advisor : ***Dr. Rafael Espinosa-Luna***

Co-Advisor : ***Qiwen Zhan, Ph.D.***

Student : ***BSc. Phys. Víctor-Manuel Rico-Botero***

July, 7th 2016
León, Guanajuato, México

Gratefulness

I only have words of gratitude with a lot of people who have believed in me and the intellectual aptitudes that supposedly I have. To write this thesis has been enjoyable to me, because when I take the decision to do graduate studies, fortunately I was accepted to the first option that I had in mind: *Optics*. It always has been interesting to me because talk about Optics is necessarily talk about Physics... and I am a lover of that knowledge area.

I want explicitly to express my gratefulness to Mexican people, to allow me through CONACyT and Centro de Investigaciones en Óptica A.C. be a scholarship holder and give me the opportunity of to know their country, their cultural heritage and share the scientific equipment and knowledge. I fell in love of this country and is still hard to believe that being a foreigner, they have given me so much that I did not found in my home country. Sincerely, thank you so much.

On the other hand, I want to extend furthermore my sincerely gratefulness to Dr. Rafael Espinosa-Luna by accept me immediately in his group when I was looking for an advisor and to professor Qiwen Zhan to provide the source idea for this work. To professor Espinosa, special thanks for to be a beauty person, patient and to attend to any person always with that smile and great disposition. It is a big teaching lesson to me. Also I am grateful with the GIPyS students: Guadalupe López-Morales, Izcoatl Saucedo-Orozco, Jason Gómez-Jamaica, and Eusebio Aguilar-Fernández for sharing with me their experiences and help me when I was searching answers. Particularly, the helpful of Guadalupe was very important to develop this work. Her previous experience at University of Dayton and her experimental skills, help me to understand and solve the main experimental problems that were present with the setup. I also extend my thanks to Dr. Sergio Calixto and Dr. Luis Felipe Lastras to review my preliminar manuscript. I am in gratitude too with a lot of people: technicians, researchers, some professors, and administrative people without which this thesis would be not written by me. To every body, thank you very much!.

Víctor Manuel Rico Botero
2016-Jul-05th

*Prefiero actuar ahora que estoy convencido,
y no tener que lastimarme después
pensando que pude hacer mucho y no hice nada.*
VMRB.

Abstract

Here we present an option to measure the refractive index of materials by using the ellipsometry technique. In the traditional method a beam of polarized light is sent, at different angles, to the materials surface where it is reflected. The state of polarization of this reflected beam is analyzed (recorded) every time a new angle is given. With these values the Fresnel reflectance graphs are obtained and the refractive index is calculated. Now we propose a method that is based on a high numerical aperture objective lens. A single recording is done. The process involves the study of the change of polarization state, associated to an incident illumination field, when it is reflected from the plane surface of the material. To perform this study the spatial distribution of light, at the pupil of the objective lens, is transferred by means of a lens to a CMOS 1280×1024 matrix detector. The image obtained as a result, contains the reflectance information at multiple and continuous local planes of incidence with a completed round. Then the distribution of light is studied with some computer programs, allowing the measurement of the Brewster angle and the deduction of the value of the refractive index associated to the area under study. In this work, the question about what kind of polarized light is the more appropriate illumination source that should be employed to obtain a measurement of the refractive index, using the technique shown here, is answered. To give a response, BK7, MgF2, FS and SF12 glasses were excited with conventional and unconventional polarization fields, and the experimental results were compared with synthetic images computed through the Fresnel theory. Results show the use of unconventional polarization provides the most complete information and allows the spatial identification of anisotropies within spot diameters around 721 nm.

Contents

1	Introduction	1
2	Fundamentals: Polarization and Ellipsometry	5
2.1	Conventional polarization	5
2.1.1	Stokes vector and Poincarè sphere	7
2.1.2	Polarization effects in materials: Mueller matrices	8
2.1.3	Making polarization sources and analyzers	8
2.2	Polarization at reflected and transmitted illumination fields	11
2.3	Quick revision about ellipsometry	12
2.3.1	Multiple angle-of-incidence ellipsometry	15
2.3.2	Measurement at Brewster's angle	16
2.3.3	Measurement of complex refractive index	17
2.4	Non conventional polarization	18
3	Experiment: getting information of optical properties at micrometric areas	21
3.1	Experimental approach	21
3.2	Sample excitation	23
3.2.1	Polarization mode converter	23
3.2.2	Samples under study	23
3.3	Image detection	25
3.4	Final experimental implementation	26
3.5	Computational codes	26
3.5.1	Cropping the experimental image to an effective area (<code>cropImage.m</code>)	27
3.5.2	Calculation of the reflectance at multiple-angle-of-incidence (<code>reflectanceAtMAI.m</code>)	29
3.5.3	Calculation of the incident electric field matrices for radial and azimuthal polarization modes (<code>rAndAV2.m</code>)	33
3.5.4	Experimental image processing and comparison between expected and theoretical images (<code>MAIguiV2.m</code> , <code>findMinimum2.m</code>) and <code>findMinimumExp.m</code>	36

4	Results and discussions	39
4.1	System calibration	39
4.2	Measurement of optical properties: Brewster's angle and refractive index	40
4.3	Discussions	41
5	Conclusions and perspectives	49
6	Appendix	53
6.1	Design of mechanical pieces	53
	Plane of general setup	53
	Plane of universal cage plate	55
	Plane of 300 mm rod	56
	Plane of 150 mm rod	57
	Plane of laser coupling	58
	Plane of retarder coupling rod	59
	Plane of lens tube couplig	60
	Plane of polarizer coupling (piece 1)	61
	Plane of polarizer coupling (piece 2)	62
	Plane of polarizer coupling (piece 3)	63
	Plane of s-waveplate coupling	64
	Plane of CMOS camera coupling	65
6.2	MatLab code for <code>cropImage.m</code>	66
6.3	MatLAB code for <code>reflectanceAtMAI.m</code>	67
6.4	MatLAB code for <code>rAndAV2.m</code>	69
6.5	MatLab code for <code>findMinimum2.m</code>	70
6.6	MatLab code for <code>findMinimumExp.m</code>	71
6.7	Technical problems and solutions	72

Chapter 1

Introduction

Quantify how many light is reflected by a surface and how is its spatial distribution, is a problem that impacts areas like optoelectronics[5, 14], the material's characterization[7] and health sciences[2]. The relevance of them is based in that reflected light contains information about the interaction between the medium properties and the incidence illumination field. Particularly, properties like refraction index and Brewster's angle, conjugated with experimental parameters like the incidence angle and rugosity, controls the amount of reflected light. From physics, this problem is approached by means of the Fresnel coefficients theory[10]. At the direct problem, if the incident electric field is known (it is, its magnitude, the polarization state and its phase) and the mathematical model that transforms this vectorial field into reflected, the amount of reflected light by the surface can be calculated. At the inverse problem, knowing the reflected and incident fields, the parameters of the system transference function can be calculated and hence some optical properties of the medium.

From the experimental point of view, several ideas looking for synthesize an instrument, that provides more details about the reflected light field given by a surface has been implemented. An interesting example about that is the Murray-Coleman and Smith proposal[16], in which reflected light distribution is obtained by means of automatic data measurements on a system pc-controlled. There making a discrete swept of angular positions of the illumination source as well as the detector, and rotating the sample at also discrete steps, is possible to get information about the surface reflectance inside of a spherical section accesible by the equipment (figure 1.1a).

Another proposal reported by Ward[25], uses a hemisphere half-silvered and a CCD camera with a fish-eye lens (figure 1.1b). In this setup, the reflected field is collected by the hemisphere and reflected back to the CCD detector. Similarly to the Murray-Coleman' system, different incident angles

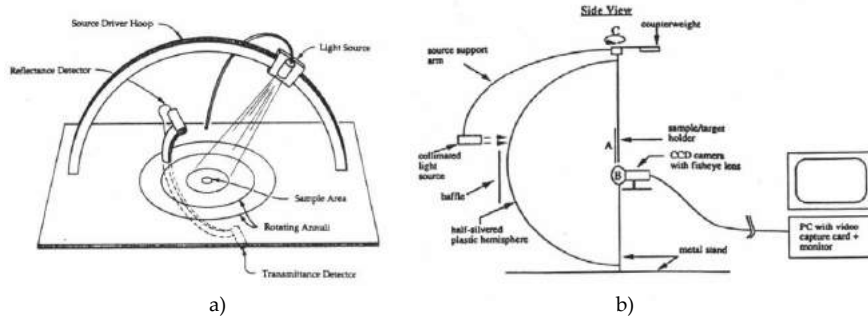


Figure 1.1: Opto-mechanical setup to measure reflectance light distribution from a sample. a) Murray-Coleman proposal[16]. b) Ward's idea[25].

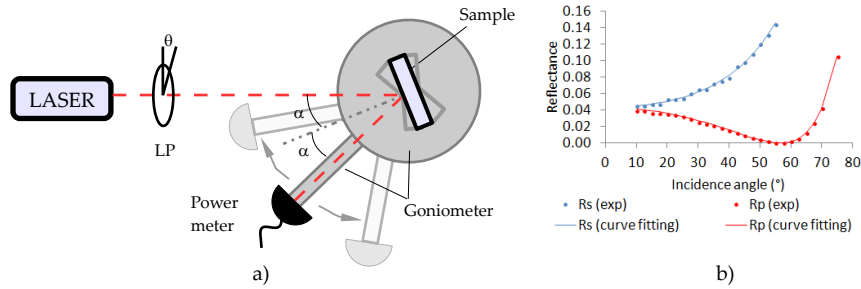


Figure 1.2: Scheme of the goniometric experiment to get reflectance curves at CIO's graduate laboratory. a) opto-mechanical setup. b) typical experimental curve obtained.

are swept automatically, controlling the zenithal height and the azimuthal orientation of the illumination source, achieving an image composition of the reflected field from each independent discrete measurements.

At CIO's graduate laboratory, an equipment with similar characteristics, but manually operated, is used to check the Fresnel coefficient theory (figure 1.2). There, a laser system aligned with a linear polarizer allow the reproduction of the reflectance values vs the incidence angle. With this method, if a light beam with a horizontal polarization is used as illumination source, the curve should reach an absolute minimum whose abscissa is known as the Brewsters angle. However, unlike to Murray-Coleman and Ward equipments, the optomechanical setup of the CIO's device, allow only the surface's reflectance studies at only one plane of incidence.

The common framework associated to the shown devices, as well as another similar equipments (like the used at NIST[17], for example), is that they can be classified as goniometric type. Those proposal are char-

acterized because its reflectance measurements are done sequentially (it is point by point) and because its operation principle implies the use of mobile pieces. The approach of the present work is about how to avoid the mobile pieces and how to get the same reflectance information but using just one step. One of the main question that the author and the advisors are looking for, is to get information, at least in qualitative form, about the isotropy of a sample. Looking for the answer, the goniometer system idea was replaced by a microscope objective lens, and the powermeter detector, used to measure the intensity at each measurement point, has been replaced by a camera obtaining hence an experimental image as result. The main idea, if polar coordinates are used to identify each pixel, is that the radial and angular position asociated to any image's point, will be informing about the incidence angle and the plane of incidence respectively, whereas the pixel intensity could be interpreted as the point's reflectance.

On the other hand, Fresnel reflectance curves obtained for instance by means of a CIO's goniometer system, are usually measured exciting the sample with linearly polarized illumination fields oriented with the plane of incidence or perpendicular to it. However, it is interesting to explore the behavior of the reflectance curves when the sample is excited with another kind of polarization, like circular (right hand or left hand) polarization states or radial and azimuthal polarization modes. Those last kind of polarization, have been playing an important role in the applications with polarized light like the engineering of optical fields[24], through which there are some ideas to generate optical needles experimentally. Our group has been working recently in this area, particularly has been reported how to generate this kind of polarization with passive elements like scattering on a thin metallic cylinder[21]. So, the present work is contributing into two ways: proposing a new experimental setup to find reflectance distribution associated to a sample, and a new application of the unconventional polarization modes.

The text is organized in five Chapters of which this introduction is the first. Later, in the Chapter 2, a brief background about the polarized light, the polarization states and a description of the polarization modes are done, to document the mathematical formalism employed in the Chapter 3, where the computational codes and the experimental arrays are shown. Chapters 4 and 5 are dedicated to show and discuss the results and the conclusions. A previous work, in which the mechanical design of optical pieces to make the optical system with laboratory pieces is documented, as well as the complete computational codes used and the documentation of optical problems and solutions that were presented along the experiment implementation.

Chapter 2

Fundamentals: Polarization and Ellipsometry

2.1 Conventional polarization

Conventional polarization states are based in the direction of the electric field oscillation and its spatial homogeneous distribution. Because the most outstanding part of an electromagnetic wave is the electrical component, electric field is usually enough to describe the polarization state of light. Suppose that the electric field associated to a plane wave, can be seen as a linear combination of the base elements,

$$V = \{\mathbf{E}_1, \mathbf{E}_2\} \quad (2.1)$$

with

$$\mathbf{E}_1 = E_1 e^{i((\mathbf{k}\cdot\mathbf{r})-\omega t+\delta_1)} \hat{\mathbf{e}}_1 \quad (2.2)$$

$$\mathbf{E}_2 = E_2 e^{i((\mathbf{k}\cdot\mathbf{r})-\omega t+\delta_2)} \hat{\mathbf{e}}_2 \quad (2.3)$$

Particularly, it has been assumed that fields are propagating in the same direction. δ_1 and δ_2 are the initial field phases, ω the field frequency, and $\hat{\mathbf{e}}_{1,2}$ are the unitary vectors along the x, y directions, respectively. An element of the V 's generated space is,

$$\mathbf{E} = \left(E_1 e^{i\delta_1} \hat{\mathbf{e}}_1 + E_2 e^{i\delta_2} \hat{\mathbf{e}}_2 \right) e^{i(\mathbf{k}\cdot\mathbf{r}-\omega t)} \quad (2.4)$$

Introducing the *phase difference factor* $\delta \equiv \delta_2 - \delta_1$, equation (2.4) can be restated as,

$$\mathbf{E} = \left(E_1 \hat{\mathbf{e}}_1 + E_2 e^{i\delta} \hat{\mathbf{e}}_2 \right) e^{i(\mathbf{k}\cdot\mathbf{r}-\omega t+\delta_1)} \quad (2.5)$$

The last expression contains the main elements associated with a conventional polarization state: field amplitudes $\{E_1, E_2\}$ and phase difference between fields $\{\delta\}$; usually, δ_1 is considered as a phase constant. Setting

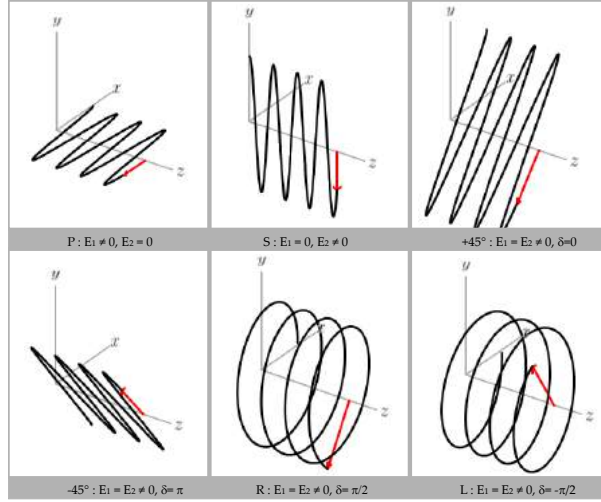


Figure 2.1: Drawing path of electric field (Eq. 2.5) when time evolution is allowed. To learn how to make its own drawings, visit author personal simulations web page[20].

the parameters $\{E_1, E_2, \delta\}$ and allowing the time evolution, a conventional polarization state is drew by the electric field. Six of that states and its corresponding parameters and shown in figure 2.1.

Some interesting aspects about the parameters $\{E_1, E_2, \delta\}$ are:

- The kind of conventional polarization {linear, circular, elliptical} is defined mainly by δ parameter. It can be controlled experimentally with optical devices named *retarder waveplates*[9].
- Ratio between E_1 and E_2 (and $\delta = 0$) also defines the kind of polarization, for example:
 - * $E_1/E_2 \approx 0 \rightarrow$ linear P polarization.
 - * $E_1/E_2 \approx \infty \rightarrow$ linear S polarization.
 - * $E_1/E_2 = 1 \rightarrow$ linear $+45^\circ$ polarization.
 - * $E_1/E_2 = -1 \rightarrow$ linear -45° polarization.

However, due that the electric field is not a physical *observable*, intensity calculus, which are observable parameters, are preferred. In that orden, the expression (2.5) is transformed to,

$$I = \mathbf{E} \cdot \mathbf{E}^* = |E_1|^2 + |E_2|^2 + E_1 E_2^* e^{-i\delta} \hat{\epsilon}_1 \cdot \hat{\epsilon}_2 + E_2 E_1^* e^{i\delta} \hat{\epsilon}_1 \cdot \hat{\epsilon}_2 \quad (2.6)$$

Considering only real field amplitudes and not necessarily orthogonal fields, then

$$I = \mathbf{E} \cdot \mathbf{E}^* = |E_1|^2 + |E_2|^2 + 2E_1 E_2 \cos(\Theta) \cos(\delta) \quad (2.7)$$

Table 2.1: Polarization states (normalized) and its corresponding field parameters. T denotes the transposed operation.

$ E_x $	$ E_y $	δ	\mathbf{S}	Pol. Type
1	0	0	$(1 \ 1 \ 0 \ 0)^T$	P
0	1	0	$(1 \ -1 \ 0 \ 0)^T$	S
1	1	0	$(1 \ 0 \ 1 \ 0)^T$	+45°
1	1	$-\pi$	$(1 \ 0 \ -1 \ 0)^T$	-45°
1	1	$\pi/2$	$(1 \ 0 \ 0 \ 1)^T$	R
1	1	$-\pi/2$	$(1 \ 0 \ 0 \ -1)^T$	L

where Θ is the angle between $\hat{\epsilon}_1$ and $\hat{\epsilon}_2$ unitary vectors.

2.1.1 Stokes vector and Poincarè sphere

Usually, any conventional polarization state associated to a monochromatic plane wave, is represented by means of a given Stokes vector which is defined as [6],

$$\mathbf{S} = \begin{pmatrix} S_0 \\ S_1 \\ S_2 \\ S_3 \end{pmatrix} = \begin{pmatrix} |E_x|^2 + |E_y|^2 \\ |E_x|^2 - |E_y|^2 \\ 2|E_x||E_y|\cos(\delta) \\ 2|E_x||E_y|\sin(\delta) \end{pmatrix} \quad (2.8)$$

Here, field directions have been set as the canonical vectors $\{\hat{\mathbf{e}}_x, \hat{\mathbf{e}}_y\}$. The meaning of each matrix element is,

- S_0 : total intensity associated to the polarization state.
- S_1 : intensity associated to the linear P (> 0) or S (< 0) polarization state.
- S_2 : intensity associated to the linear +45° (> 0) or -45° (< 0) polarization state.
- S_3 : intensity associated to the circular R (> 0) or L (< 0) polarization state.

The six polarization states shown in figure 2.1 are described in table 2.1. Normalized matrix elements $\{S_1, S_2, S_3\}$ are plotted as coordinate points on the *Poincarè sphere*, where the normalized intensity represents the unitary radius. That plot allows to show graphically the polarization state:

- Points on equator represents linear polarization states.
- Points on sphere poles defines circular polarization states.

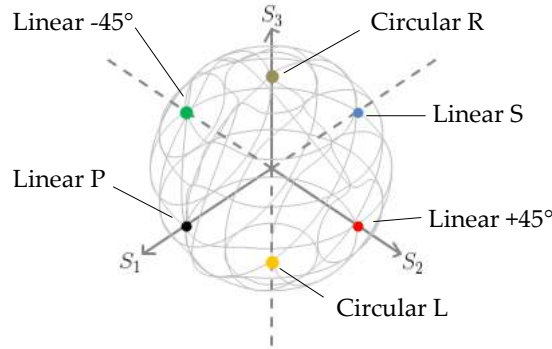


Figure 2.2: Poincaré sphere and representation of the main polarization states.

- Points out of equator and sphere poles define elliptical polarization states.

Poincaré sphere and polarization states described in table 2.1, are shown in figure 2.2. Two special polarization states not represented in figure 2.2 are: $\mathbf{S}_{\text{un}} = (1 \ 0 \ 0 \ 0)^T$ and $\mathbf{S}_{\text{null}} = (0 \ 0 \ 0 \ 0)^T$. They are named *unpolarized* and *null* polarization states, respectively. It means that illumination field represented by them, does not has a defined polarization state (in the first case) and there is not an illumination field present (in the other one)[6].

2.1.2 Polarization effects in materials: Mueller matrices

In nature, there are materials that change the polarization states linearly. Analytically these materials act as *operators* on the polarization state and are represented by the called *Mueller Matrices*, which have a 4×4 dimension. The interaction of an illumination field with a material that transforms its polarization state, can be expressed mathematically as,

$$\mathbf{S}^o = \hat{M}\mathbf{S}^i \quad (2.9)$$

Where \mathbf{S}^o and \mathbf{S}^i represent the output and input polarization state respectively, and \hat{M} is the Mueller matrix associated with the material's linear effect. Mueller matrices associated to some special optical devices are shown in table 2.2.

2.1.3 Making polarization sources and analyzers

With the Mueller matrices described in table 2.2, it is possible (analytical and experimentally) to develop equipment enabled to make and to analyze

Table 2.2: Ideal Mueller matrices associated to special optical devices[6, 9]. θ indicates the angle of device's principal axis respect to a horizontal line, and δ is the phase difference or retarder factor between waves traveling along the slow and fast axis.

Device	Mueller matrix
Linear horizontal polarizer	$\frac{1}{2} \begin{pmatrix} 1 & \cos(2\theta) & \sin(2\theta) & 0 \\ \cos(2\theta) & \cos^2(2\theta) & \sin(2\theta)\cos(2\theta) & 0 \\ \sin(2\theta) & \sin(2\theta)\cos(2\theta) & \sin^2(2\theta) & 0 \\ 0 & 0 & 0 & 0 \end{pmatrix}$
General retarder	$\begin{pmatrix} 1 & 0 & 0 & 0 \\ 0 & \cos^2(2\theta) + \cos(\delta)\sin^2(2\theta) & \frac{1}{2}(1 - \cos(\delta))\sin(4\theta) & -\sin(\delta)\sin(2\theta) \\ 0 & \frac{1}{2}(1 - \cos(\delta))\sin(4\theta) & \sin^2(2\theta) + \cos(\delta)\cos^2(2\theta) & \sin(\delta)\cos(2\theta) \\ 0 & \sin(\delta)\sin(2\theta) & -\sin(\delta)\cos(2\theta) & \cos(\delta) \end{pmatrix}$
Half wave-plate	$\begin{pmatrix} 1 & 0 & 0 & 0 \\ 0 & \cos(4\theta) & \sin(4\theta) & 0 \\ 0 & \sin(4\theta) & -\cos(4\theta) & 0 \\ 0 & 0 & 0 & -1 \end{pmatrix}$
Quarter waveplate	$\begin{pmatrix} 1 & 0 & 0 & 0 \\ 0 & \cos^2(2\theta) & \sin(2\theta)\cos(2\theta) & -\sin(2\theta) \\ 0 & \sin(2\theta)\cos(2\theta) & \sin^2(2\theta) & \cos(2\theta) \\ 0 & \sin(2\theta) & -\cos(2\theta) & 0 \end{pmatrix}$

polarization states. That can be achieved by smart setups that involve the use of linear polarizers and waveplates or phase retarders and hence operations with Mueller matrices. The use of a polarimetric setup on axis, implies Mueller matrix multiplication, whereas a parallel polarimetric setup leads to a Mueller matrix sum.

Particularly using just a non polarized light source and a linear polarizer, makes possible to generate any linear polarization state setting the polarizer to an specific azimuthal angle (figure 2.3a and 2.3d). Otherwise, elliptical, circular right-hand, circular left-hand, and linear P polarization states, can be generated adding a quarter waveplate (QWP) in series and after to a linear polarizer (figure 2.3b and 2.3e). On the other hand, if a linear polarized light source (for example a typical illumination field originated from a linear polarized laser) should be rotated, the use of a single half waveplate is enough to perform that transformation (figure 2.3c and 2.3f).

The most general setup to generate any conventional polarization state, is by means of a linear polarizer, a half waveplate and a quarter waveplate in on axis setup, which is called a *Polarization State Generator* (PSG)[8]. A PSG is shown in figure 2.4, the arrangement consist of the following optical devices, properly mounted into azimuthally rotating mechanical mounts: linear polarizer + half waveplate+quarter waveplate. Linear polarizer + half waveplate, define a linear polarized state rotated at an angle defined by the orientation of the half waveplate's fast axis. The function of the

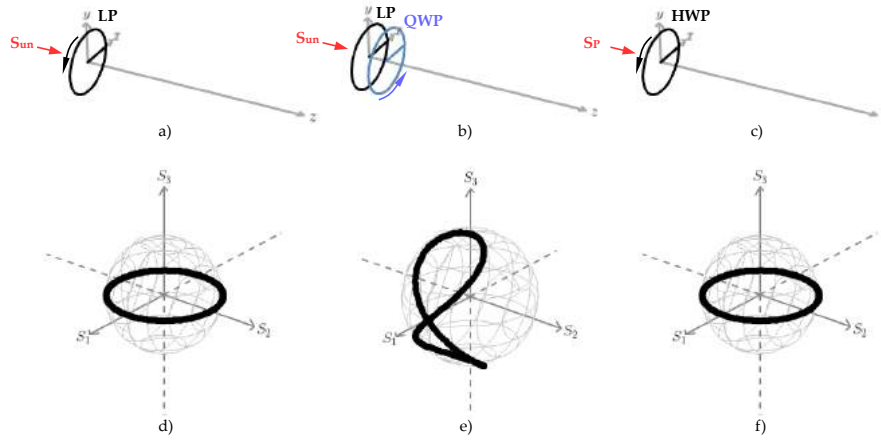


Figure 2.3: Generation of conventional polarization states. Schematic diagrams for: a) linear polarization using non polarized light source; the device represented is a linear polarizer, b) elliptical polarization using non polarized light source: the black device is a linear polarizer whereas the blue element is a quarter waveplate, c) linear polarization using a linearly polarized light source; the device represented is a half waveplate. Curves described on the Poincaré sphere when is turned on: d) the linear polarizer of the array a), e) quarter waveplate of the array b), and f) the half waveplate of the array c).

quarter waveplate is to transform linear to elliptical polarization state. Then choosing an appropriated angle's set for half waveplate and quarter waveplate, it is possible transform, for instance unpolarized light to any conventional polarization state (figure 2.3). It can be seen on the Poincaré sphere, like the “eight” figure, which is drew by rotation of the quarter waveplate and its position (azimuthal angle on equator) is controlled by the half waveplate.

On the other hand, the most general setup to analyze any conventional polarization state, is using a quarter waveplate, a half waveplate and a linear polarizer (in that order). That array is named *Polarization State Analyzer* (PSA) and sample light travels from quarter waveplate to linear polarizer (figure 2.5). With a PSA is possible the determination of each element of a Mueller matrix by means of total light intensity given by the term S_0^o (equations 2.8 and 2.9). Playing with specific combinations of incident polarization state and polarization state analyzers, their elements can be calculated via linear equations system[9].

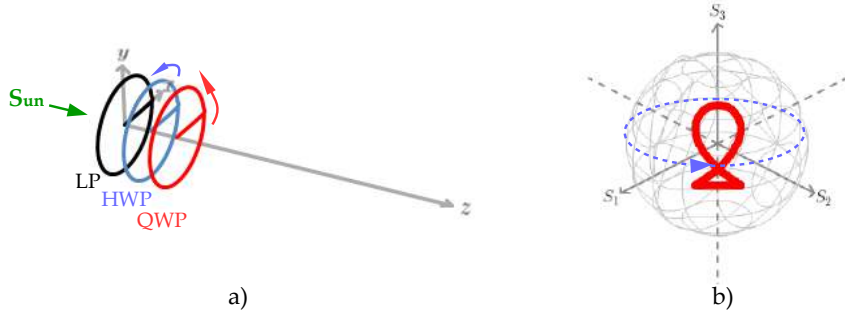


Figure 2.4: Polarization state generator (PSG). a) Experimental setup. b) Path on Poincaré sphere when optical devices (marked by arrows on setup) are rotated.

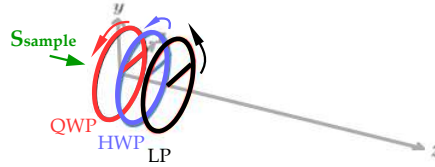


Figure 2.5: Setup for a polarizer state analyzer (PSA).

2.2 Polarization at reflected and transmitted illumination fields

Another way to generate polarized light (probably the easier according to the equipment required) is by means of reflection phenomena. According to Fresnel theory, the interaction of an illumination field with a surface separating two optical media, generates elliptically polarized light both under reflection and refraction field[10]. The polarization state made in this form, is highly dependent on the physical properties of the media involved and the incidence angle. In the case of dielectrics, where refractive index is a real quantity, it is described by the following set of exact equations,

$$\Gamma_P = \left(\frac{\tan(\theta_i - \theta_t)}{\tan(\theta_i + \theta_t)} \right)^2 \quad (2.10)$$

$$\Gamma_S = \left(\frac{\sin(\theta_i - \theta_t)}{\sin(\theta_i + \theta_t)} \right)^2 \quad (2.11)$$

$$T_P = \frac{\sin(2\theta_i) \sin(2\theta_t)}{\sin^2(\theta_i + \theta_t) \cos^2(\theta_i - \theta_t)} \quad (2.12)$$

$$T_S = \frac{\sin(2\theta_i) \sin(2\theta_t)}{\sin^2(\theta_i + \theta_t)} \quad (2.13)$$

where Γ and T symbols represents *reflectance* and *transmittance* quantities, P and S sub-index the kind of polarization asociated to each term, θ_i the incidence angle and θ_t the refracted angle. Due to refracted angle follows the Snell's law ($\theta_t = \sin^{-1}(n_t/n_i \sin(\theta_i))$), these expressions have a dependency with the refractive index, so the interaction of incident light with characteristic optical medium properties, make slight¹ changes detectable in the mathematical plot used to describe this situation. Figure 2.6 shows the behavior of equations (2.10) to (2.13) to some specific refractive index. It should be noted that with a real refractive index, light is not extinguished whereas travels into the material and a conservative system behavior is gotten. As a result of the energy conservation principle, each reflectance curve is complementary with its correspondent transmittance plot, which involves that the amount of energy missing from a curve to reach the unity can be found in the other curve of the same polarization nature. On the other hand, the incidence angle where Γ_P plot goes to zero (see zoom insert), is named *Brewster's angle*.

In the case of metals, a complex refractive index ($\tilde{n} = n + i\kappa$) and therefore an extinction coefficient (κ) should not be neglected. In that case, reflectance quantities are described by the following set of equations[9, 6],

$$\Gamma_P \approx \frac{\left(n - 1/\cos(\theta_i)\right)^2 + (n\kappa)^2}{\left(n + 1/\cos(\theta_i)\right)^2 + (n\kappa)^2} \quad (2.14)$$

$$\Gamma_S \approx \frac{\left(n - \cos(\theta_i)\right)^2 + (n\kappa)^2}{\left(n + \cos(\theta_i)\right)^2 + (n\kappa)^2} \quad (2.15)$$

Here an approximation symbol has been used due to the condition $\tilde{n}^2 \gg \sin^2(\theta_i)$ is employed in its derivation[9]. Figure 2.7 shows the behavior of equations (2.14) and (2.15) to some specific complex refractive indexes. Similarly, in this case reflectance curve reaches a minimum value, but in contrast with the dielectric case, it does not achieve to be zero. That incidence angle is called *pseudo-Brewster's angle*.

2.3 Quick revision about ellipsometry

The analysis of polarization states generated via reflection of an illumination field at a surface is known as *ellipsometry*[13]. By definition, equations (2.10) to (2.13) describe how the intensity of an illumination field changes

¹slight word is used in this context due to Γ and T plots at different refractive index, differ only in 5% or less. Plots at Figure 2.6, has intentional zoom to do more explicit such effects.

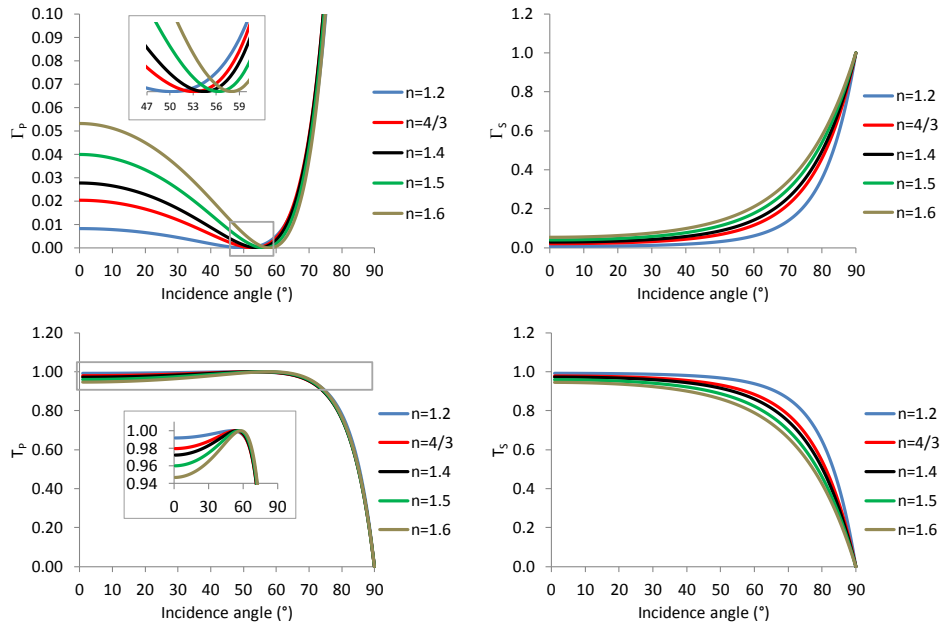


Figure 2.6: Reflectance (Γ) and transmittance (T) curves for parallel (sub-index P) and perpendicular (sub-index S) polarization states at different refractive index.

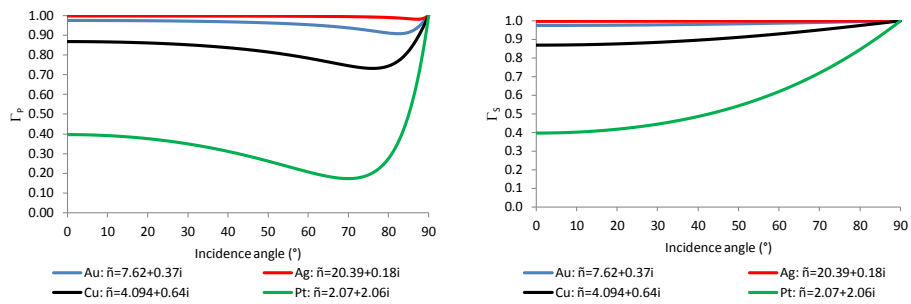


Figure 2.7: Reflectance curves for parallel (sub-index P) and perpendicular (sub-index S) polarization states for some metals at different incident angles and complex refractive indices. \tilde{n} values are taken from [18]

under reflection and transmission at each P and S polarization states; the Γ_P term for example, that is the ratio between P polarized reflected and incident intensities. However, as shown by equation (2.8), a polarization state instead of its intensity, can be defined in terms of amplitudes and phase difference between two orthogonal electric field components, and the equation set (2.10) to (2.13) does not provide explicitly information about that. In the reflection case, it can be interesting to know not only what is going on with reflectance at P and S polarization state separately, but how a reflectance (Γ_P for example) affects the other (Γ_S) and how is the phase relationship at different linear polarization states. Ellipsometry deals with it.

To illustrate how ellipsometry works, let the incident field amplitudes be represented as,

$$E_P = E_{(0P)}e^{i\alpha_P} \quad (2.16)$$

$$E_S = E_{(0S)}e^{i\alpha_S} \quad (2.17)$$

and the reflected fields,

$$R_P = R_{(0P)}e^{i\beta_P} \quad (2.18)$$

$$R_S = R_{(0S)}e^{i\beta_S} \quad (2.19)$$

Here, α and β are symbols used to indicate the phase of each field, which are not equal in the most general case. That yields to a not usual form of Fresnel coefficients, in which reflection terms are given by,

$$\rho_m \equiv \frac{R_m}{E_m} = \frac{R_{(0m)}}{E_{(0m)}}e^{i(\beta_m - \alpha_m)} \quad m = \{P, S\} \quad (2.20)$$

A ratio between P and S reflection terms allows to obtain a special expression that has, in a single equation, amplitudes and phase factors. It is known as *relative amplitude attenuation*(ρ) and is given by[1],

$$\rho \equiv \frac{\rho_P}{\rho_S} = \frac{R_{(0P)}E_{(0S)}}{R_{(0S)}E_{(0P)}}e^{i(\beta - \alpha)} \quad (2.21)$$

where $\beta \equiv \beta_P - \beta_S$ and $\alpha \equiv \alpha_P - \alpha_S$.

Usually due the P and S polarization states are referred to orthogonal electric fields, quotient of amplitudes preceeding Euler symbol can be interpreted as rate of change or a tangent of an angle denoted ψ ; furthermore which value given by $\beta - \alpha$ means the net phase difference between incident and reflected fields, usually that difference is replaced by Δ . Then, equation (2.21) is rewritten as,

$$\rho = \tan(\psi)e^{i\Delta} \quad (2.22)$$

Last expression is known as *the fundamental equation of ellipsometry*[9]. The main goal in this area is at the experimental side: to measure ψ and Δ parameters, and at the theoretical side: to find a functional relationship of these parameters with the optical properties (mainly refractive index n , absorption coefficient k and thin film thickness d) of the sample where the incident illumination field is reflected.

2.3.1 Multiple angle-of-incidence ellipsometry

Curves shown in figures 2.6 and 2.7 can be obtained point to point analyzing the intensity of a reflected light beam with a linear polarizer, and measuring its value with a powermeter to different angles at P and S polarization directions. However, obtaining experimental reflectance curves via this method can be a long procedure, time delays and measurements accuracy could not be ensured, mainly because each measured point is registered at different times and stability of optical parameters and illumination source in some systems can be hard to guarantee. To solve that, instead of a single illumination beam, excitation with a multiple and *continuous* angle-of-incidence (or MAI) can be performed and a measurement's image is obtained as result.

To achieve the multiple angle of incidence, usually a focused beam is guided to the sample under study so that in a single step, the sample is irradiated at different angles. Choosing a particular beam convergence (or numerical aperture, NA), an angle range between $\theta = 0$ and $\theta = \sin^{-1}(NA)$ is swept. To focus the illumination field, a high numerical aperture objective lens is typically employed. High numerical aperture is a key characteristic to ensure that Brewster's angle (minimum value in Γ_P plot at figure 2.6) is cover-up. To collect the image of the reflected field, experimental setups similar to the sketch of the figure 2.8a are usually employed[27, 22]. A non-polarizing beam splitter is used here to *split* the incident from the reflected beams of light. In the special case when only linear P and homogeneous polarization is used to irradiate (figure 2.8b), different kind of polarization orientation are experimented by the sample; it is an effect of the focussing field, in which the direction of the incidence plane varies with the azimuthal angle at the objective lens, while linear polarization direction of irradiation field stays constant. It implies that not always the irradiation field is contained into the local plane of incidence and so, reflectance and transmittance phenomena should be exposed. Where the sample experiences linear P polarization illumination field at Brewster's angle, as is predicted by the Fresnel coefficients (equations (2.10) and (2.11)), the reflected field should be extinguished and black zones at reflected image will appear (figure 2.8c).

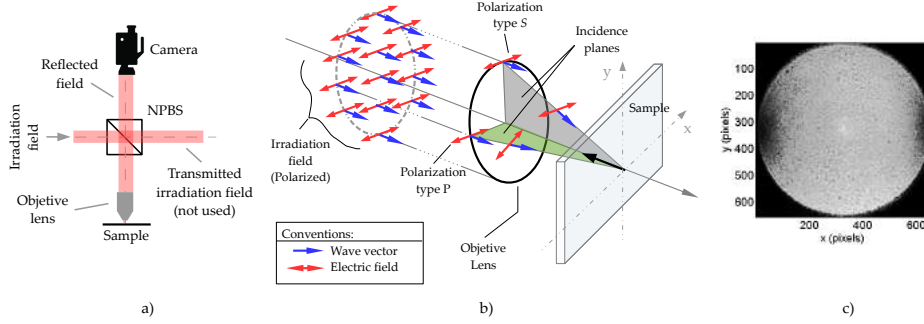


Figure 2.8: a) Sketch of a typical microellipsometry setup; a non-polarizing beam splitter is employed to *splits* the irradiation field of the reflected. b) Behavior of P polarized illumination field when is focused into a objective lens; due that the direction of the incidence plane changes with the azimuthal angle and the linear polarization direction stays constant, to some azimuthal angles the incident polarization field is in the incidence plane (P polarization state) and to others do not. c) Theoretical image that should be obtained as reflected field. Black zones corresponds to angles where linear P polarized light is extinguished because the linearly P -polarized wave incides at the Brewster angle associated to the surface under study.

2.3.2 Measurement at Brewster's angle

Ellipsometry allows to get a quick measurement of Brewster's angle of a sample, identifying the position of extinguished light zones. According to the idea presented in figure 2.8, each radii-vector traced from the center until any image's point, is associated to an angle of incident and a combination of P and S reflectance values. To illustrate it, in figure 2.9a the effect of focusing the irradiation field until the sample is shown; the objective lens employed is represented here through θ_{max} (parameter that depends of numerical aperture NA). Knowing the pupil radii R of the reflected (and collimated) field, focal distance can be calculated using trigonometry,

$$f = \frac{R}{\tan(\theta_{max})} = \frac{R}{\tan\left(\sin^{-1}\left(\frac{NA}{n_a}\right)\right)} \quad (2.23)$$

Here, n_a is the refractive index of the media between objective lens and the sample.

In the same way, the relation between an arbitrary distance of image's center (the radii r , $r < R$) and the incidence angle (θ) can be calculated as,

$$\theta(r) = \tan^{-1}\left(\frac{r}{f}\right) \quad (2.24)$$

so, in an image like figure 2.8c, radii measurements indicates -through the last equation- the incidence angle. To plot the entire image, just the vectorial

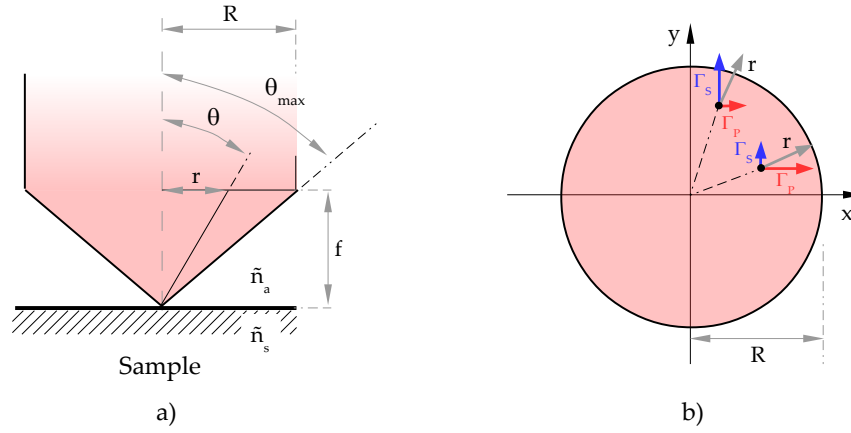


Figure 2.9: a) Side view of a collimated illumination field focused into a sample material; \tilde{n}_a and \tilde{n}_s denote environmental and sample complex refractive indices respectively. b) Transversal cut of reflected field; each image's point has associated P and S reflectance values that depend of its azimuthal angle.

sum of Γ_P and Γ_S is developed to each position (figure 2.9b). Using image processing, Brewster's angle can be calculated identifying the position of light extinguished zones.

2.3.3 Measurement of complex refractive index

To measure the complex refractive index from the image obtained as a reflected field (figure 2.8c), there are at least two ways:

1. By means of Brewster's angle and the refractive index relation: $\tan(\theta_B) = n_s/n_a$; measuring θ_B and knowing n_a , n_s is immediately found.
2. By means of ellipsometric parameters ψ and Δ .

The first method implies a quick and easy calculation of the Brewster's angle measurement, however as is shown, just the real part of the refractive index ($\tilde{n} = n + ik$) can be calculated.

The second option has been marked as more accurate[13], but it involves the use of polarimetric devices to analyze the polarization state of the reflected field. To perform it, there are several methods[13, 1], one of them named *principal angle method* is as follows:

Let a linear $+45^\circ$ polarized light be illuminating, in the most general case, a metallic surface at an angle θ (figure 2.10). As an effect of the reflection, there are a phase factor between the P and S components of the reflected

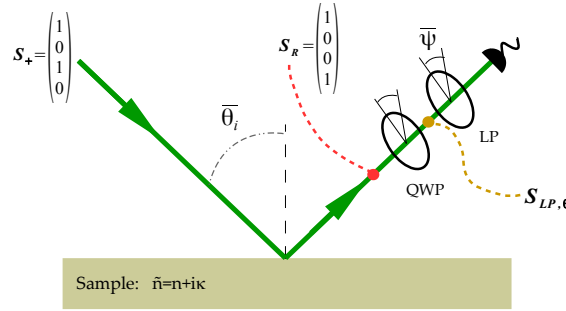


Figure 2.10: General setup and main idea of the principal angle of incidence method. Finding $\bar{\theta}_i$ and $\bar{\psi}$ angles, complex refractive indexes can be measured.

field that have a dependence with the incidence angle². Particularly, exists an angle of incidence that will be denoted as $\bar{\theta}_i$, where the phase difference is $\pi/2$ and then the polarization state generated is of the kind circular right hand. That angle is named *Principal Angle of Incidence* and the polarization state generated is denoted as *standard*[9]. The reflected field is passed through a quarter wave plate and a linear polarization state is obtained, however its polarization angle is unknown. To get it, reflected field is passed through a linear polarizer and rotated until the illumination field is extinguished. The angle where that condition is achieved is named *Principal Azimuthal Angle* and will be denoted as $\bar{\psi}$. Measuring $\bar{\theta}_i$ and $\bar{\psi}$ the complex refractive parameters can be determined by means of the following equations[6]:

$$n = -\sin(\bar{\theta}_i) \tan(\bar{\theta}_i) \cos(2\bar{\psi}) \quad (2.25)$$

$$\kappa = \tan(2\bar{\psi}) \quad (2.26)$$

2.4 Non conventional polarization

In contrast with conventional polarization where the electric field follows a spatially homogeneous distribution, the polarization state is (ideally) the same at any point of the illumination field, non conventional polarization is described via distributions of spatially non homogeneous electric field and the meaning of polarization state migrates to *polarization modes*. To show how mathematically it works, the electric field component associated

²it is the main goal of ellipsometry. A brief explanation to this phenomena, is that on the one hand, one part of the incident linear $+45^\circ$ polarized light (the normal component of the P polarized illumination field), tries to excite charges displacement at the direction where the symmetry is broken, and on the other hand if exist material anisotropy charges, displacement are not necessarily equal along each direction.

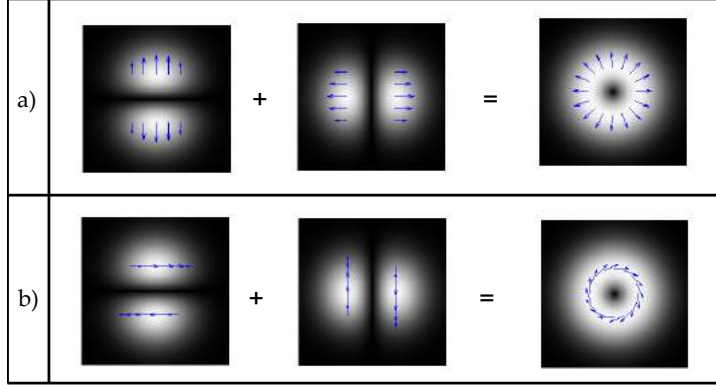


Figure 2.11: Representation of radial (a) and azimuthal (b) polarization modes. $u_{m,n}(x, y, z)$ controls the field amplitude distribution. The modes presented here (and other modes) can be obtained by assigning a polarization direction (P or S) to each distribution and adding them together.

to an illumination field, can be shown as composed by an amplitude's field distribution $u(x, y, z)$, a propagator term, and a field direction, it is,

$$\mathbf{E} = u(x, y, z)e^{i(\omega t - \mathbf{k} \cdot \mathbf{r})} \hat{\mathbf{e}}_j \quad (2.27)$$

Depending of the reference coordiante system employed, the amplitude field distribution can be an expression that involves, for rectangular coordinates, the *Hermite-Gauss* polynomials (H_i)[29],

$$u_{m,n}(x, y, z) = AH_m\left(\sqrt{2}\frac{x}{w(z)}\right)H_n\left(\sqrt{2}\frac{y}{w(z)}\right)\frac{w_0}{w(z)}e^{-i\phi_{mn}(z)}e^{-\frac{k}{2q(z)}(x^2+y^2)} \quad (2.28)$$

and for cylindrical coordinates the *Laguerre-Gauss* polynomials (equation 2.29), where (L_p^l) or the *Bessel of the first kind* polynomial (J_0) when rotational symmetry is considered (equation 2.30)[29],

$$u(r, \phi, z)_{l,p} = A\left(\sqrt{2}\frac{r}{\omega}\right)^l L_p^l\left(2\frac{r^2}{\omega^2}\right)\frac{w_0}{w(z)}e^{-i\varphi(z)_{lp}(z)}e^{-\frac{k}{2q(z)}r^2} \quad (2.29)$$

$$u(r, z) = A\frac{w_0}{w(z)}e^{-i\varphi(z)}e^{-\frac{k}{2q(z)}r^2} J_0\left(\frac{\beta r}{1 + iz/z_0}\right) \quad (2.30)$$

In these equations, A is a field amplitude constant, $\omega(z)$ is the beam size, ω_0 is the beam size at beam waist, $\phi_{mn}(z) = (m + n + 1)\tan^{-1}(z/z_0)$ (for rectangular coordinates) and $\varphi(z) = (2p + l + 1)\tan^{-1}(z/z_0)$ (for cilindrical coordinates) are the Gouy phase shift, k the wavevector, $q(z)$ is the complex beam parameter, β is a scaling parameter, J_0 is the 0^{th} order Bessel function of the first kind and $i = \sqrt{-1}$.

Playing with the order of the polynomials ($\{m, n\}$ for rectangular coordinates or $\{l, p\}$ for cylindrical coordinates), a lot of amplitude's field distribution can be obtained[28], however just the most lower modes of the

Hermite-Gauss polynomials are particularly interesting in this work, that is, the modes $\{m, n\} = \{(0, 1), (1, 0)\}$.

It can be shown that superposing the Hermite-Gauss amplitude's field distribution $u_{1,0}(x, y, z)$ and $u_{0,1}(x, y, z)$, two special orthogonally polarized modes called *radial polarization mode* (equation 2.31 and figure 2.11a) and *azimuthal polarization mode* 2.32 and figure 2.11b) are obtained[29]. The graphical illustration of these modes are shown in the figure 2.11.

$$\mathbf{E}_r = u_{1,0}\hat{\mathbf{e}}_x + u_{0,1}\hat{\mathbf{e}}_y \quad (2.31)$$

$$\mathbf{E}_\varphi = u_{0,1}\hat{\mathbf{e}}_x + u_{1,0}\hat{\mathbf{e}}_y \quad (2.32)$$

Chapter 3

Experiment: getting information of optical properties at micrometric areas

3.1 Experimental approach

To get optical properties of materials like complex refractive index and its characteristic Brewster's angle, a multiple angle of incidence microellipsometer was set. The schematic diagram of the optical assembly is shown on figure 3.1. The array is similar to a confocal microscope, in the sense that employs an objective lens to focus a plane of interest and a beam splitter to redirect reflected light to a detector (a camera), however a pin hole (key piece for confocal microscopes) is not used here[26]. The foundation of this setup, is to get in just one step the reflected light observed at different angles of incidence from an object under study and hence to obtain information about its optical properties. To analyze how an illumination field travels in this array, consider that a collimated and polarized light beam reaches the non-polarizing beam splitter (NPBS). There, the illumination field is partially reflected to an objective lens; the transmitted portion is spread to a region where that light is not used. With an appropriate linear displacement, the beam reflected by the NPBS is focused into the sample under study, and as an effect of the reflection, the illumination field is returned by the same path but in the opposed direction of the beam splitter; this effect is shown with more detail in figure 3.1b. Then the NPBS reflects one portion of the returned field in direction to the illumination source, and the other one is transmitted to the camera detector. Between the NPBS and the objective

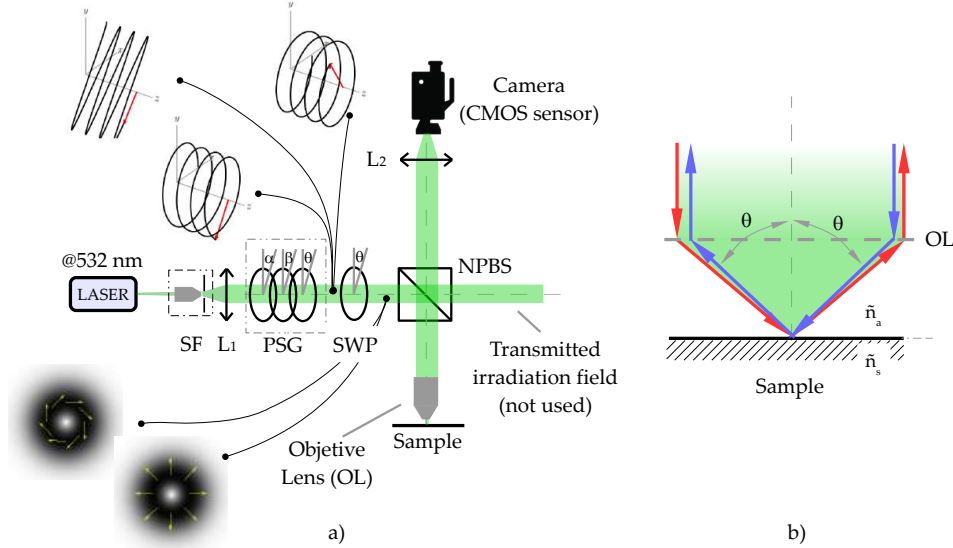


Figure 3.1: a) Schematic diagram for the experimental setup: SF spatial filter, L_1 collimating lens, PSG polarization state generator, SWP s-waveplate, NPBS non polarizing beam splitter, L_2 image forming lens. b) Effect of the objective lens when a collimated light is focused into a sample material; the returned illumination field travels in the same path of the incident beam but in opposite direction.

lens as well as the NPBS and the illumination source, probably¹ an interference effect (of the type standing waves) occurs, but due that it is local, that effect is neglected. To ensure collimation, a Petzval objective formed by the lenses L_1 and L_2 is employed. A lens L_3 is furthermore employed to form an image of the returned field into the camera sensor. A polarization state generator (PSG) formed by the set of a linear polarizer (LP), a half waveplate (HWP) and a quarter waveplate (QWP) is employed to excite the sample with different kind of conventional polarization states. In the same way a polarization state analyzer (PSA) formed by the set of a QWP, a HWP and a LP is used to analyze the polarization of the returned illumination field. A special device called a *S-waveplate* allows to transform linear to radial or azimuthal polarization[19] and hence enable the experimental setup to evaluate the behavior of the sample when is excited with non conventional polarization. To ensure collimation, a collimation test was done using the shearing interferometer Thorlabs SI254[23]. The test was done before capturing experimental images. The shearing interferometer was located in the camera beam arm.

¹It is depending of the light polarization. To obtain interference is needed that waves have the same polarization state.

3.2 Sample excitation

The illumination at multiple angles of incidence is achieved by means of an objective lens, which focuses a light field into an interest region. As was described at 2.3.1, using a high numerical aperture objective lens, could ensure that the Brewster's angle of the sample is cover-up and hence dark zones appear in the image registered by the detector. The role of the PSG in the experimental array, is allow to set diferent kind of polarization states as illumination source. Experimentally it is reached fitting the three PSG's devices (LP, HWP, and QWP) at specific orientations. As was shown at figure 2.8, exciting with linearly polarized light, appear symmetrical dark zones at specific positions where the Γ_P^2 coefficients gets the minimum value. On the other hand, if linear polarization is rotated, the Γ_P^2 coefficient achieves the minimum value at other position and therefore, the observed effect is that dark zones are rotated too. Finally, as circular polarization is just a linear polarization superposition that changes its orientation with the time, it should be expected that instead of two symmetrical dark zones, a smooth dark ring appears around the center of the image. This ring is expected as smooth darkness and not as strongest, due to for each azimuthal angle, the darkness appear in just one position whereas for other azimuthal angles, the same position will be illuminated.

3.2.1 Polarization mode converter

To excite the sample with unconventional polarization modes, a linear to radial/azimuthal polarization converter (*S-waveplate*) has been employed. This device has a femtosecond laser machined nanostructure that vary spatially the phase to produce radial and azimuthal distributions of electric field as well as polarization vortex[4]. Due that the effective working area of the S-waveplate is 6 mm[19], the beam overall setup's path has been defined to be close to this diameter. The manual given by the manufacturer of the S Waveplate indicates that to produce radial polarization, the S-waveplate's alignment mark should be oriented *parallel* to an incident linear polarization and for azimuthal polarization the mark should be oriented *perpendicular*. However, an experimental evaluation of that condition revealed that it is necessary to get an angle of 45° between the alignment mark and the incident linear polarization to obtain the right mode.

3.2.2 Samples under study

To choose appropriate samples, two main criteria have been applied:

- Sample's Brewster's angle should be less than the angle covered by the objective lens. It can be calculated via numerical aperture (NA):
-

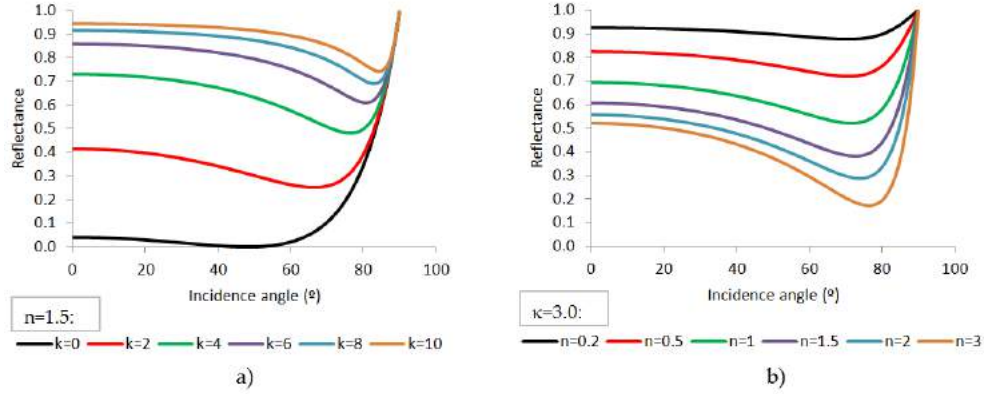


Figure 3.2: Reflectivity curves for: a) some extinction coefficient (κ) values keeping the real part of the complex refractive index fixed. b) some refractive index (n) values keeping the imaginary part of the complex refractive index fixed

$\theta_{max} = \sin^{-1}\left(\frac{NA}{n_a}\right)$, where n_a is the refractive index of the medium between the objective lens and the sample.

- For non dielectric samples, the contrast between reflected intensity at angles far from the pseudo-Brewster's angle and the intensity at pseudo-Brewster's angle was stronger, to ensure that it was solved by the camera sensor. This corresponds to materials with the complex part (the extinction coefficient) bigger as well as the real part (the refractive index)².

Dielectric samples could be the most easiest to evaluate due that in dielectrics at the Brewster's angle the intensity reaches zero values. However for non dielectric samples at that angle, the intensity reaches just a minimum (but not zero) value and for some materials (like gold for example) the contrast between reflectivity near and far of the Brewster's angle is poor. This analysis is shown in figure 3.2 where the real and imaginary part of the complex refractive index is adjusted to simulate the behavior of the materials with these parameters³.

According to the criteria discussed before and the list of optical properties of materials shown in the table 3.1, samples like NaF , MgO , CaF_2 or Al_2O_3 results are adequate if an objective lens with a numerical aperture of 0.9 is used. The consolidated material's list of the table 3.1 has been selected due that they are not exotic materials and furthermore because they have a complex refractive index reported at a wavelength near to 532 nm, the central wavelength of the laser employed in this work.

²It would be a material with an exotic dispersion curve, where taking the Brewster's angle as reference, the reflectivity is high before and after that angle but small closer to

Table 3.1: Complex refractive index values and its characteristic Brewster's angle. n and κ have been taken from [18]. Brewster's angle (θ_B) has been calculated by means of $\tan^{-1}(n)$.

Material's name	Chem. Formula	n	κ	$\lambda(nm)$	θ_B
Sodium Flouride	NaF	1.32684		530.0	53.0
Magnesium oxide	MgO	1.74390	6.55	514.5	60.2
Magnesium oxide	MgO	1.74077		546.1	60.1
Calcium fluoride	CaF_2	1.43575		520.0	55.1
Calcium fluoride	CaF_2	1.43512		540.0	55.1
Aluminium oxide	Al_2O_3	1.77300		516.7	60.6
Aluminium oxide	Al_2O_3	1.77100		539.1	60.5
Hexagonal cobalt	Co	2.05000	3.82	548.6	64.0
Berylium	Be	3.30000	3.18	516.6	73.1
Berylium	Be	3.39000	3.17	563.5	73.6
Tantalum	Ta	2.68000	1.92	516.6	69.5
Tantalum	Ta	2.56000	1.86	563.5	68.7
Chromium	Cr	2.98000	4.45	532.1	71.4
Potassium	K	0.04600	1.28	506.1	2.6
Potassium	K	0.04900	1.43	546.2	2.8
Sodium	Na	0.06300	2.07	506.1	3.6
Sodium	Na	0.05900	2.23	546.2	3.4

3.3 Image detection

To record an image of the returned illumination field, a CMOS camera has been employed. To ensure that all of the information present at the illumination field is impinging at the camera sensor, a convergent lens has been employed too. To perform the image's polarization analysis, a PSA can be used. Essentially, recording the P -reflectance (Γ_P) and the S -reflectance (Γ_S), an image of the ρ parameter (equation 2.21) can be obtained, and hence the refractive index map of the sample's illuminated area. According to the objective lens manufacturer[11], the spot diameter at focal distance is given by following equation:

$$\phi_f = 1.22 \frac{\lambda}{NA} \quad (3.1)$$

With $NA = 0.9$ and $\lambda = 532 \text{ nm}$, the spot diameter is $\phi_f \approx 721 \text{ nm}$.

it.

³This simulation can be accessed at[20]

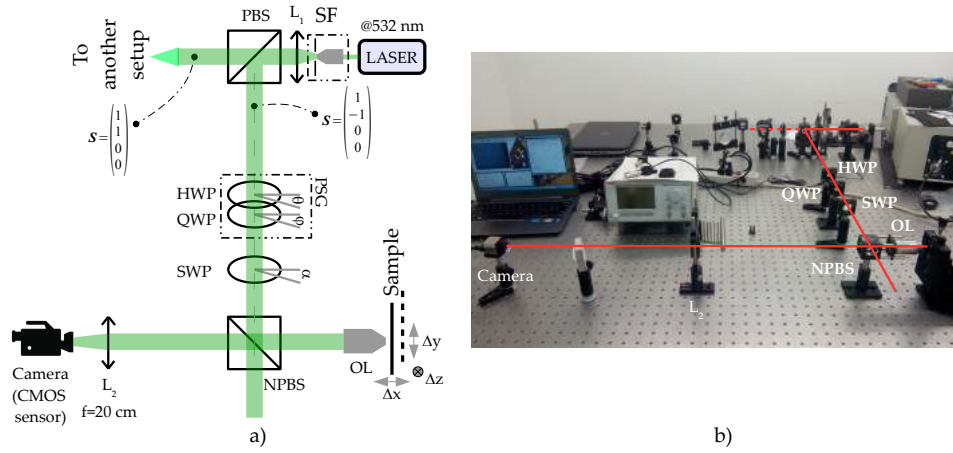


Figure 3.3: a) Schematic diagram of experimental setup finally implemented. b) Setup at GIPyS laboratory. SF: spatial filter, L_1 and L_2 : convergent lenses, PBS: polarized beam-splitter, HWP: half waveplate, QWP: quarter waveplate, SWP: s-waveplate, NPBS: non polarizing beam-splitter, OL: objective lens.

3.4 Final experimental implementation

At laboratory, the multiple angle-of-incidence microellipsometer was implemented as is shown in the figure 3.3. To optimize the use of laboratory equipment, a non polarized laser source was splitted in two polarized beams. To achieve that, the beam is spatially filtered and a polarized beam splitter (PBS) was employed, being the vertical (or type S) polarization assigned to the array here discussed. Once the beam is polarized, the first device of the PSG (the linear polarizer) was removed and then the PSG is composed just by the linear retarders (HWP and QWP) decreasing the experimental degree of freedom of the light source from three until two.

To facilitate alignment and allowing the exploration of several sample's areas, the sample was ensambled on a x, y, z micrometric translational stage. That element is a key piece to ensure that the first surface of the sample is focused by the objetive lens (OL). When focusing is performed and if the incident beam is collimated, the returned illumination field is collimated too. Table 3.2 shows the final list of equipment employed and its main characteristics.

3.5 Computational codes

To get information from the experimental image observed at laboratory and compare it with the equivalent image expected, a set of MatLAB computational codes was wrote. The most general program is a graphical user interface that invoque subrutines for the development of specific calculus.

Table 3.2: List of optical devices employed at the implementation of the multiple angle-of-incidence microellipsometer.

Item	Brand	Reference	Description
1	Thorlabs	CPS532	Laser diode module (532 nm, Div=0.5 mrad)
2	Newport	910A	Compact Five-Axis Spatial Filter ($40x - 10\mu m$)
3	Thorlabs	CM1-PBS251	Polarized beam splitter (420 nm - 680 nm)
4	Thorlabs	AHWP05M-600	Half waveplate
5	Thorlabs	AQWP05M-600	Quarter waveplate
6	Altechna	any	S-waveplate
7	Thorlabs	CM1-BS013	Non polarized beam splitter, 50:50
8	Nikon	any	Objective lens (TU Plan Fluor 100x/NA=0.9)
9	Thorlabs	AHWP05M-600	Half waveplate
10	Thorlabs	AHWP05M-600	Quarter waveplate
11	CIO	any	achrom. doubl. for camera, $f = +20\text{ cm}$
12	CIO	any	collimating lens, $f = +5\text{ cm}$
13	Thorlabs	DCC3240C	CMOS camera, 1280×1024 pixels, Sensor size

Those subrutines, were written in the MatLAB version R2009a, and are compiled as numerical functions. The first step to use the program, is to load through the graphical user interface, an experimental image obtained with the microellipsometer of multiple angle-of-incidence (figure 3.3). Then, the image is processed digitally and based in its size, a theoretical (or synthetic) image is calculated. The engineering below of these codes, its explanation and how to execute them are shown in the following sections.

3.5.1 Cropping the experimental image to an effective area (cropImage.m)

Due that the most probably experimental situation is that the image captured at laboratory is not centered at the camera sensor, and the useful information is just a fraction of the entire file given the vision system, an image cropping algorithm, named `cropImage.m`, was wrote. Figure 3.4 shows a comparison between an experimental image observed at laboratory and the cropped image delivered by the computational code. Its operation principle is shown below.

The input parameters for this program are,

- **image**: the matrix associated to the experimental image captured at laboratory. This matrix should be monocromatic (at one color, is to say: just one matrix).
- **contrast_**: sensibility for the border detection.
- **xCroppingError**: manual adjustment for horizontal cropping.

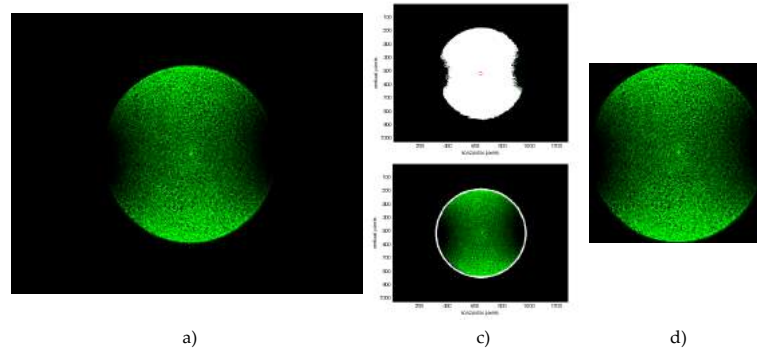


Figure 3.4: Documentation of the operation principle for `cropImage.m`: a) Experimental image example without cropping processing. b) identification of neighboring pixels with high contrast (above) and identification of the interest area. c) Experimental image example with cropping processing.

- `yCroppingError`: manual adjustment for vertical cropping.

As execution result, the computational code gives a square matrix for the image cropped, so that the interest illumination field covers most of the image.

The code begins calculating the numerical derivate for the image. Due that the experimental image matrix has numbers in the range $[0, 1023]^4$, neighboring pixels with a higher intensity difference, shows higher values in its derivate⁵, allowing the border identification. Pixels where the derivate is bigger than the parameter `contrast_` are marked, and the coordinates for those pixels are captured. It is shown in the following code lines:

```

1  dAdx=diff(sourceImage');           % image derivate
2  xBorder=dAdx>contrast_;           % higher contrast ident.
3  [x,y]=find(xBorder);             %

```

Due that a lot of neighboring pixels satisfy the condition set at line 2, but all of these points are inside of the interest area, the center of the image can be calculated as the mean position of the points with higher contrast,

```

4  x_bar=mean(x);                   % x-average position
5  y_bar=mean(y);                   % y-average position

```

To determine the points where the image will be cropped, a circle with center (x_bar, y_bar) is calculated. The circle's radii is calculated by means of the extremes position of the high contrast points.

⁴the experimental images were taken with a camera sensor working at 10 bit.

⁵In this context, the derivate operator is reduced to a simple difference between neighboring pixels. Mathematically, the derivate is defined as $\frac{df}{dx} = \lim_{h \rightarrow 0} \frac{f(x+h) - f(x)}{h}$. In this case $h = 1$ pixel, then $\frac{df}{dx} = f(x+1) - f(x)$.

```

6  theta=0:2*pi/100:2*pi; %
7  r=max((y_bar-min(y)),x_bar-min(x)); %
8  xC=r*cos(theta)+x_bar+xCroppingError; %
9  yC=r*sin(theta)+y_bar+yCroppingError; %

```

then, the image cropped at the circle's cardinal points. The matrix `croppedImage` is the element exported when the code is invoked.

```

10 croppedImage=double(imcrop(sourceImage,[min(xC),...
11                          min(yC),2*r,2*r]));

```

3.5.2 Calculation of the reflectance at multiple-angle-of-incidence (reflectanceAtMAI.m)

To produce the image expected with the microellipsometer of multiple angle-of-incidence for a sample with particular optical properties, a calculation based on the Fresnel coefficients was done. To make the calculus, matrices for the sample's refractive index map and the incident electric field are prepared previously to the application of the Fresnel coefficients. This matrices are squared and have the same resolution of the experimental image loaded. For the sample under study, a customizable refractive index value with a tolerance range, is supplied as a scale factor of a homogeneous matrix preloaded with a 1 at each element, namely:

$$n_s = (n \pm \delta n) \begin{pmatrix} 1 & \cdots & 1 \\ \vdots & \ddots & \vdots \\ 1 & \cdots & 1 \end{pmatrix} \quad (3.2)$$

For the incident electric field, matrices for its horizontal and vertical components are calculated. When the sample is excited with conventional polarization, the Jones parameters E_x , E_y and δ set by the user, scale a homogeneous matrix preloaded with a 1 at each element as follows:

$$E_x^i = E_x \begin{pmatrix} 1 & \cdots & 1 \\ \vdots & \ddots & \vdots \\ 1 & \cdots & 1 \end{pmatrix} e^{i\delta}, \quad E_y^i = E_y \begin{pmatrix} 1 & \cdots & 1 \\ \vdots & \ddots & \vdots \\ 1 & \cdots & 1 \end{pmatrix} \quad (3.3)$$

On the other hand, when the sample is excited with unconventional polarization, the matrices E_x^i and E_y^i are loaded with the Hermite-Gauss distributions (equation 2.28). Those matrices are calculated through the program `rAndAV2.m`. The program begins by calculating the maximum incidence angle swept by the objective lens and its focal distance (equation 2.23). Then a coordinate matrix and the distance from each point of them at the coordinate origin is calculated.

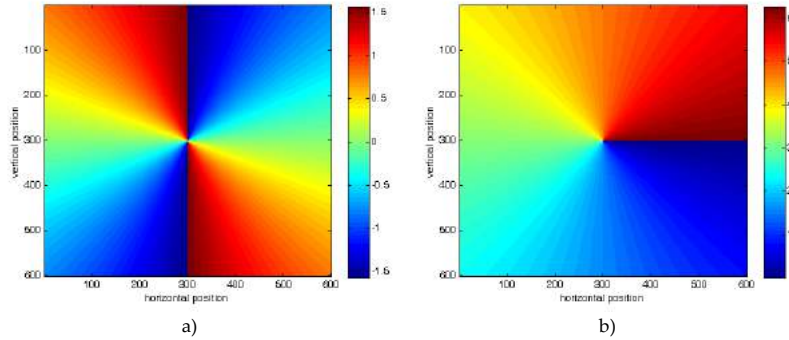


Figure 3.5: Azimuthal angle for the objective lens. a) without quadrant complement calculation. b) with quadrant complement calculation

```

1  rho=300;                               % image radii
2  thetaMax=asin(NA);                       %
3  f=rho/tan(thetaMax);                     % focal distance
4  pixelsVector=linspace(-rho,rho,2*rho); %
5  [x,y]=meshgrid(pixelsVector);           % coordinate matrix
6  r=sqrt(x.^2+y.^2);                       % distance matrix
    
```

Later, the angle (φ) of each point of the coordinate matrix respect to the horizontal axis is calculated via $\varphi = \tan^{-1}(y/x)$. This calculation show a technical problem when it is performed directly, due that the coordinates x and y are defined in the interval $-\text{rho} \leq (x, y) \leq \text{rho}$, ($\text{rho} > 0$), and arc-tangent function makes a jump from $\pi/2$ to $-\pi/2$ or viceversa when there is a change of sign in any coordinate (x or y), which causes a discontinuous azimuthal angle matrix for the objective lens. To solve that, the angle calculation is complemented to each quadrant. Figure 3.5 show the images of the azimuthal angle with and without the quadrant complementation, respectively.

```

7  cuadrantI=(x>=0)&(y>=0);                 %
8  cuadrantII=(x<0)&(y>=0);                %
9  cuadrantIII=(x<0)&(y<0);                %
10 cuadrantIV=(x>=0)&(y<0);                %
11 phyI=atan(y./x).*cuadrantI;             %
12 phyII=(atan(y./x)+pi).*cuadrantII;      %
13 phyIII=(atan(y./x)+pi).*cuadrantIII;    %
14 phyIV=(atan(y./x)+2*pi).*cuadrantIV;    %
15 phy=phyI+phyII+phyIII+phyIV;           %
    
```

Later, depending of the type of polarization employed (conventional or unconventional), the horizontal and vertical electric field matrices are calculated.


```

16  switch polType                                %
17      case 'conv'                               %
18          Ex=E_x*ones(length(x),length(y))*exp(1i*delta); %
19          Ey=E_y*ones(length(x),length(y));    %
20      case 'unconv'                             %
21          [Ex,Ey]=rAndAV2('r',632E-9,12,0,1.6); %
22  end                                           %

```

In the same form, the angle (α) associated to the electric field at each point of the coordinate matrix is calculated as $\alpha = \tan^{-1}(E_y/E_x)$. As before, to avoid discontinuities in this matrix, the angle calculation is complemented again to each quadrant but usign as a cuadrant reference the place where the horizontal and vertical components of the electric field takes positive and negative values.

```

23  ExPositive=Ex>0;                             %
24  ExNegative=Ex<0;                             %
25  EyPositive=Ey>0;                             %
26  EyNegative=Ey<0;                             %
27  alphaI=atan(Ey./Ex).*ExPositive.*EyPositive; %
28  alphaII=(atan(Ey./Ex)+pi).*ExNegative.*EyPositive; %
29  alphaIII=(atan(Ey./Ex)+pi).*ExNegative.*EyNegative; %
30  alphaIV=(atan(Ey./Ex)+2*pi).*ExPositive.*EyNegative; %
31  alpha=alphaI+alphaII+alphaIII+alphaIV;       %
32  alpha=alpha';                               %

```

At this point, the magnitude of the incident electric field is calculated.

```

33  E=sqrt(Ex.*conj(Ex)+Ey.*conj(Ey));          %

```

Due that for a given incident electric field, the more general situation is that a piece of it is on the incidence plane and the other piece is perpendicular to that plane, it is necessary to decompose the incident electric field ($\mathbf{E}^i = E_x^i \hat{\mathbf{e}}_x + E_y^i \hat{\mathbf{e}}_y$) into its parallel (E_p^i) and perpendicular (E_s^i) components to the plane of incidence (figure 3.6). The parallel electric field component is calculated by the inner product of the incident electric field with the unitary vector pointing from the coordinate origin to point where the incident electric field is analyzed. It can be expressed mathematically as,

$$E_p^i = \mathbf{E}^i \cdot \hat{\mathbf{r}} = E^i \cos(\varphi - \alpha) \quad (3.4)$$

Once the parallel component has been determinated, the perpendicular electric field component can be calculated as the module of the vectorial subtraction between the incident electric field and its parallel component,

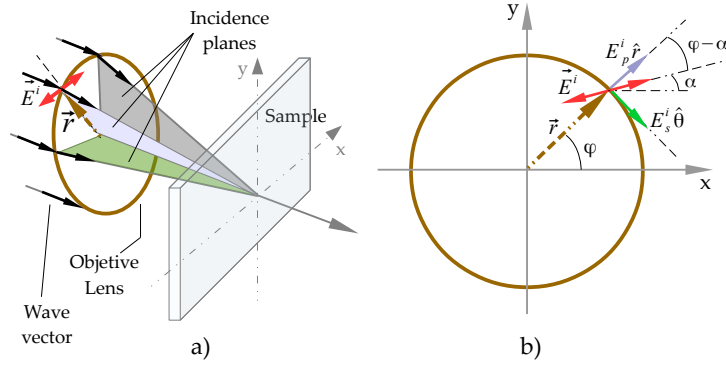


Figure 3.6: Incident electric field and its decomposition into parallel and perpendicular fields to the plane of incidence. a) 3D view. b) frontal view: if the incident electric field has an orientation angle α respect to the x axis, then it is forming an angle $\varphi - \alpha$ with the plane of incidence.

it is:

$$E_s^i = \|\mathbf{E}^i - E_p^i \hat{r}\| \quad (3.5)$$

Due that $\mathbf{E}^i = E^i (\cos(\alpha)\hat{e}_x + \sin(\alpha)\hat{e}_y)$ and $\hat{r} = \cos(\varphi)\hat{e}_x + \sin(\varphi)\hat{e}_y$, then:

$$E_s^i = \sqrt{(E_i \cos(\alpha) - E_p^i \cos(\varphi))^2 + (E_i \sin(\alpha) - E_p^i \sin(\varphi))^2} \quad (3.6)$$

The respective computational lines are then,

```

34 Ep_i=E.*cos((phy-alpha)); %
35 Es_i=sqrt((E.*cos(alpha)-Ep_i.*cos(phy)).^2+... %
36           (E.*sin(alpha)-Ep_i.*sin(phy)).^2); %
    
```

Next, the refractive index map is calculated. As it was discussed before, this image is calculated as a homogeneous matrix with a little variation around the central value.

```

37 theta_i=atan(r/f); % incidence angle
38 n=n_s*ones(size(theta_i)); % Refractive index map
39 n=n+tol*rand(size(theta_i))-tol*rand(size(theta_i)); %
    
```

With all the previous information, the Fresnel coefficients as well as the reflected fields are calculated.

```

40  theta_t=asin(1./n.*sin(theta_i));           %
42  r_p=(tan(theta_i-theta_t)./tan(theta_i+theta_t)); %
43  r_s=-(sin(theta_i-theta_t)./sin(theta_i+theta_t)); %
44  r_p(isnan(r_p))=((n(1)-1)/(n(1)+1));       %
45  r_s(isnan(r_s))=((n(1)-1)/(n(1)+1));       %
46  Ep_r=r_p.*Ep_i;                           %
47  Es_r=r_s.*Es_i;                           %

```

The program shown in this item, has the Jones parameters $\{E_x, E_y$ and $\delta\}$ as well as the central refractive index value, its tolerance, the polarization type and the numerical aperture value as input parameters. The program gives as output parameters the matrices for the reflected fields: E_p^r and E_s^r . The execution syntax is given by:

```
[Ep_r,Es_r]=reflectanceAtMAI(E_x,E_y,delta,polType,n_s,NA,tol)
```

An execution example is,

```
[Ep_r,Es_r]=reflectanceAtMAI(1,1,0,'unconv',1.6,0.7,0.1);
```

Figure 3.7 shows some reflectance images generated by means of the program. It can be observed that the null zones are not significantly visible when the sample is excited with a circular polarization source. It is an expected result given that for circular polarization, the electric field is rotating and the null zones that appear for an instant t , are overlapped with the images generated at other times, when the null zones appear in other positions. On the other hand, due that images made with MatLAB grows the matrix index from top to bottom (for the vertical index) and from left to right (for the horizontal index), the first quadrant is located at the bottom right of the image and the angles are increased in the clockwise sense. Hence, the $+45^\circ$ linear polarization is shown here as making an angle below of the horizontal axis, or like the polarization state is observed from the source.

3.5.3 Calculation of the incident electric field matrices for radial and azimuthal polarization modes (rAndAV2.m)

To simulate the profile image for unconventional polarization modes (line 21 at `reflectanceAtMAI.m`), was wrote the computational code `rAndAV2.m`. The input parameters for this code are:

- `polType`: a string that redirects the algorithm to calculate a specific kind of polarization mode and supporting only the values 'r' for the radial case and 'a' for azimuthal case.
- `lambda`: the wavelength of the radiation source.
- `w0`: the width at the beam waist.
- `z`: the axial position where the illumination field will be drawn.

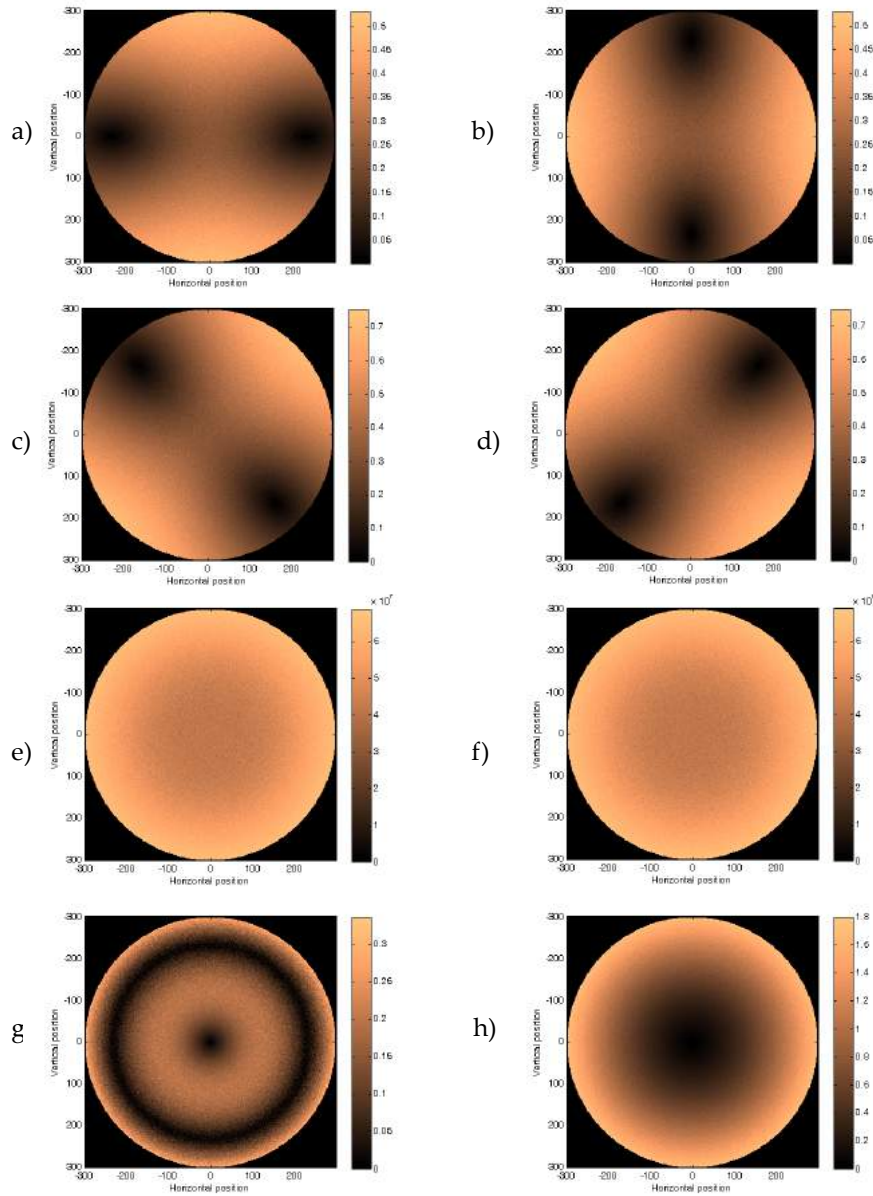


Figure 3.7: Synthetic images generated through the program `reflectanceAtMAI.m`. The images were calculated for the following parameters: $NA = 0.9$, $n = 1.6 \pm 0.1$ and an incident electric field with polarization: a) linear horizontal, b) linear vertical, c) linear $+45^\circ$, d) linear -45° , e) circular right-hand, f) circular left-hand, g) radial mode and h) azimuthal mode.

- E0: the scale factor for the amplitude of the electric field.

As output parameters, the program gives the horizontal and vertical electric field distributions. These distributions are shown as squared matrices.

The program begins by making a grid for the horizontal and vertical coordinates and calculates: the wave vector (\mathbf{k}), the beam width (wz), the radii associated to the wavefront (Rz) at the position indicated by the user, the complex beam parameter (qz) and the Gouy phase (phy).

```

1  rho=300; %
2  pixelsVector=linspace(-1,1,2*rho); %
3  [x,y]=meshgrid(pixelsVector*2E7*lambda); %
4  k=2*pi/lambda; % Wavevector
5  z0=(k*w0^2)/2; % Rayleigh length
6  wz=w0*sqrt(1+(z/z0)^2); % Beam width
7  Rz=z*(1+(z0/z)^2); % Radii of wavefront
8  Rz(isnan(Rz))=1E10; % NaN removal for z=0
9  qz=z+1i*z0; % Complex beam parameter
10 m=0; % Hermite-Gauss order
11 n=1; % Hermite-Gauss order
12 phy=(1+m+n)*atan(z/z0); % Gouy phase

```

Due that the unconventional polarization uses the Hermite-Gauss polynomials, but the main interest for this work is the study with the lowest energy modes, only the polynomials $H_0(\xi)$ and $H_1(\xi)$ are calculated. These polynomials are defined as[3]:

$$H_0(\xi) = 1 \quad (3.7)$$

$$H_1(\xi) = 2\xi \quad (3.8)$$

According to the equation (2.28) this polynomials are evaluated, depending of the polarization mode used, into the $\sqrt{2}x$ and y coordinates. Then, the Hermite-Gauss polynomials are reduced in this case to the following code lines:

```

13 h0=1; % Hermite polynomial h0
14 h1_y=2*sqrt(2)*y/wz; % Hermite polynomial h1(y)
15 h1_x=2*sqrt(2)*x/wz; % Hermite polynomial h1(x)

```

Finally, the horizontal and vertical electric field distribution are calculated.

```
16 E01=E0*w0/wz*h1_y.*exp(-1i*phy).*exp(-(x.^2+y.^2)*k/(2*qz)); %
17 E10=E0*w0/wz*h1_x.*exp(-1i*phy).*exp(-(x.^2+y.^2)*k/(2*qz)); %
18 switch polType %
19     case 'r' %
20         Ex=E01; %
21         Ey=E10; %
22     case 'a' %
23         Ex=-E10; %
24         Ey=E01; %
25 end %
```

3.5.4 Experimental image processing and comparison between expected and theoretical images (MAIguiV2.m, findMinimum2.m) and findMinimumExp.m

The theoretical image generated by the program `reflectanceAtMAI.m` and the experimental image obtained after being cut (program `cropImage.m`), are used by the graphical user interface (program `MAIguiV3.m`) to identify the position of the Brewster's angle for the sample. In both cases, the search of the absolute minimum value at the interest illumination area, allows the calculation of the characteristic Brewster's angle and hence its refractive index. For the synthetic image, the minimum values are found through computational code `findMinimum2.m`, that is given by the following lines:

```
1 rho=imageDiameter/2; %
2 pixelsVector=linspace(-rho,rho,imageDiameter); %
3 [x,y]=meshgrid(pixelsVector); % posit. matrix
4 r=sqrt(x.^2+y.^2); % dist. matrix
5 minValue=min(min(A(r<rho))); %
6 idx=find(A==minValue); %
7 [ix,iy]=ind2sub(size(A),idx); %
```

`A` and `imageDiameter` are input parameters that mean the synthetic image's distribution and the diameter of the interest illumination area respectively. At line 5, the absolute minimum value is found inside of the interest circular area, and at lines 6 and 7 its position coordinates are calculate. Although the Brewster's angle for the synthetic image can be calculated through the refractive index value, was preferred to use a minimum finder algorithm to ensure that the absolute minimum position match with an existing pixel. As output parameters, the program gives the coordinates (`[ix,iy]`) of the absolute minimum values.

For the experimental image, the position of the absolute minimum values

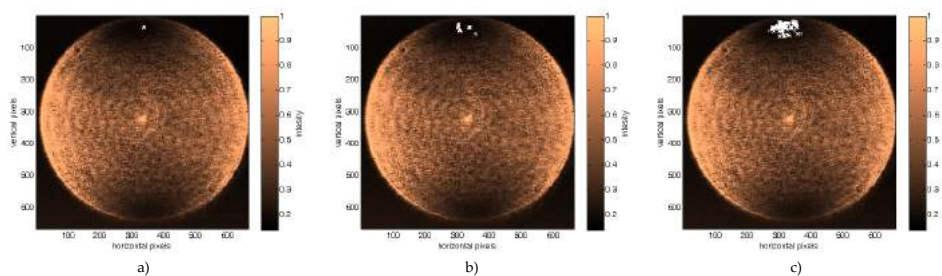


Figure 3.8: Program `findMinimumExp.m` working for an experimental image with a minimum intensity tolerance of: a) 1 pixel, b) 10 pixels, c) 20 pixels.

are calculated following the same idea, but considering a tolerance range in minimum intensity value. The computational code for it (`findMinimumExp.m`), is as follows,

```

1 rho=imageDiameter/2; %
2 pixelsVector=linspace(-rho,rho,imageDiameter); %
3 [x,y]=meshgrid(pixelsVector); % posit. matrix
4 r=sqrt(x.^2+y.^2); % dist. matrix
5 minValue=min(min(A(r<rho))); %
6 lowerLimit=(r<rho)& image>=minValue; %
7 upperLimit=(r<rho)& image<(minValue+epsilon); %
8 idx=find(lowerLimit & upperLimit); %
9 [ix,iy]=ind2sub(size(A),idx); %

```

As before, `A` and `imageDiameter` are input parameters. Here, `epsilon` is an extra input parameter that is defined through the graphical user interface. In the same form, as output parameters, the program gives the coordinates (`[ix,iy]`) of the absolute minimum values. Figure 3.8 shows program `findMinimumExp.m` working for some different tolerance conditions.

As was commented before, synthetic and experimental images and its processing job, are meet at a graphical user interface that allows to control for the synthetic image, the simulation conditions (illumination field parameters and refractive index of the sample) and for the experimental image the tolerance of minimum finding and cropping properties. With that information the squared error surface between experimental and theoretical results, as well as the matching parameter (χ^2) and the Brewster's angle and refractive index found are shown. A characteristic to allow exportation of synthetic images has been provided to further works. A screenshot of the graphical user interface is shown at figure 3.9. The original MatLAB codes for the programs shown before as well as the code for the graphical user interface are attached at sections 6.2 to 6.6. The following table summarizes

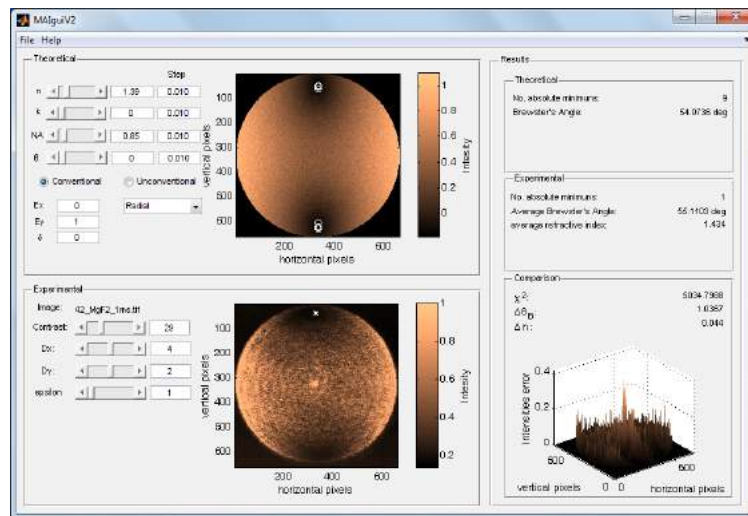


Figure 3.9: MAIguiV2 (Multiple angle-of-incidence graphical user interface) screenshot.

the programs written.

Table 3.3: Programs developed and their general description.

Program's name	Description
<code>cropImage.m</code>	Crop the image where there are interesting information
<code>reflectanceAtMAI.m</code>	Evaluates the equations (2.14) and (2.15)
<code>rAndAV2.m</code>	Generates radial and azimuthal distributions of electric field
<code>findMinimum2.m</code>	Localizes the absolute minimum of the synthetic image
<code>findMinimumExp.m</code>	Localizes the absolute minimum of the experimental image
<code>MAIguiV2.m</code>	Sets the GUI behavior

Chapter 4

Results and discussions

The computational codes and the experimental setup described at chapter 3, were used to measure the refractive index and the characteristic Brewster's angle for two kind of samples: a set of different optical glasses, and a thin film sample deposited over a microscope slide plain. For the Brewster's angle, the experimental results were compared with the theoretical angle given by the refractive index. With the experimental Brewster's angle, the experimental refractive index was calculated and its value was compared with the theoretical result given by the dispersion formula at each sample (4.1)

Table 4.1: Theoretical and experimental calculations for results comparison

Theory	Experiment
$n \xrightarrow{\theta_B = \tan^{-1}(n)} \theta_B$	$\theta_B \xrightarrow{n = \tan(\theta_B)} n$

4.1 System calibration

To calibrate the system, the experimental image obtained from a reference sample (a BK7 glass), was used to determine the effective numerical aperture of the system. According to the manufacturer, the numerical aperture for the objective lens used is 0.9. However, the effective experimental value can be near to that number, mainly because the complete optical system can contribute with a pupil that limits the observation area. Due that the dispersion formula for BK7[12] is given by,

$$\begin{aligned} n^2 &= 1 + \frac{B_1 \lambda^2}{\lambda^2 - C_1} + \frac{B_2 \lambda^2}{\lambda^2 - C_2} + \frac{B_3 \lambda^2}{\lambda^2 - C_3} \\ B_1 &= 1.03961212, C_1 = 0.00600069867, \\ B_2 &= 0.231792344, C_2 = 0.0200179144, \\ B_3 &= 1.01046945, C_3 = 103.560653 \end{aligned} \tag{4.1}$$

Table 4.2: Samples used at the multiple angle-of-incidence experiment and its theoretical Brewster's angle and refractive index

Type	Material	θ_B	$n(532 \text{ nm})$
Glass	BK7	56.6502	1.519472*
Glass	FS	55.6043	1.4607**
Glass	SF12	58.8531	1.654658*
Thin film	MgF_2	54.1732	1.385170***

source

*Shott[12]. **Malitson[15]. ***Palik[18]

at $\lambda = 532 \text{ nm}$ the refractive index is $n(532 \text{ nm}) = 1.519472 \pm 0.000005$. Setting that value as the refractive index of the theoretical image at the graphical user interface (MAIguiV2.m), the effective numerical aperture was found adjusting its value until the experimental Brewster's angle was near to $\theta_B = \tan^{-1}(1.519472) \approx 56.6502^\circ$. The effective numerical aperture found for the objective lens was then 0.85.

4.2 Measurement of optical properties: Brewster's angle and refractive index

With the system calibrated, the Brewster's angle and the refractive index for dielectric samples were measured. The samples used and its theoretical optical properties are shown at table 4.2. Each sample was excited with the six conventional polarization states (P,S,+,-,r,l) and with radial and azimuthal unconventional polarization modes. The images for the experimental results, the theoretical images, and its difference surfaces are shown at figures 4.1, 4.2, 4.3, respectively. The experimental Brewster's angle and the refractive index measured for the samples, for each polarization as well as the relative measurements errors respect to the theoretical values, are shown at figure 4.4. A graphical summary of the results given in the figure 4.4, are shown in the figure 4.5. There, an identity curve has been plotted to show which experimental refractive index points are below or above of the expected value. The distance from each point to the line is a quantification of the absolute error. To ensure a better measurement and avoid false minimum detection due to the experimental speckle, a tolerance of 5 gray levels was taken and the average of the Brewster's angle and refractive index found is shown as result. The position of the null points inside of the tolerance gray values are shown at the experimental images with white marks. The sum of squared error (χ^2) between the theoretical and experimental images are shown too at the same table. To evaluate what kind of polarization source give the better agreement between expected and measured values, a metric based on the squared error sum asociated to each plot of the figure 4.5 has been

calculated. That results are shown in the figure 4.6. A color cell background has been associated to each χ^2 value.

4.3 Discussions

To measure how similar are the experimental and the theoretical images, the metric χ^2 has been calculated. This metric is defined as the intensities sum of the squared error image (figure 4.3). Due that the intensities of the image are normalized and in this work the processed images have a typical size of approximately 600×600 pixels, the largest difference that could be quantified by this metric is $\chi^2 = 360000$. That value corresponds to a hypothetical scenario where one image (the experimental, for example) is fully saturated and the other (the theoretical, for example) is fully nulled. According to this reasoning, the closest result between the experimental and theoretical images, has been found for the sample MgF_2 excited with S polarization. The value of the metric χ^2 found by this experiment, implies that the expected and observed images differ in approximately 1.60%. On the other hand, the farthest result has been found for sample MgF_2 excited with azimuthal polarization. The value of the metric χ^2 found for this experiment, implies that the expected and observed images differ in approximately 26.33%. There are several experimental factors that are necessary to control, to ensure that the theoretical and the experimental images be closest. Some of them are itemized below:

- The exposition time: a long exposition time saturates the image and a short exposition time trouble the null zones identification. However only if the minimum position is required (it is, neglecting information about the light distribution), a saturated image is preferred.
- The refractive index distribution: samples with a non-homogeneous refractive index distribution, could show, when are excited with linear polarization for example, a set of local minima instead of a well defined absolute null zones, however in the theoretical images only a homogeneous refractive index map with a little tolerance has been simulated.
- The speckle contribution: although the speckle observed at experimental images can be attributed to the sample's rugosity, the tolerance in the sample's refractive index value contributes to that effect. This situation was simulated at figure 3.7, where a random tolerance of 0.1 for the refractive index map was considered at each pixel. With this condition, the theoretical image shows speckle.
- The sample's isotropy: for isotropic samples, two well defined and diametrically opposed null zones should appear when a linear and homogeneous polarized light is used as an illumination source. However,

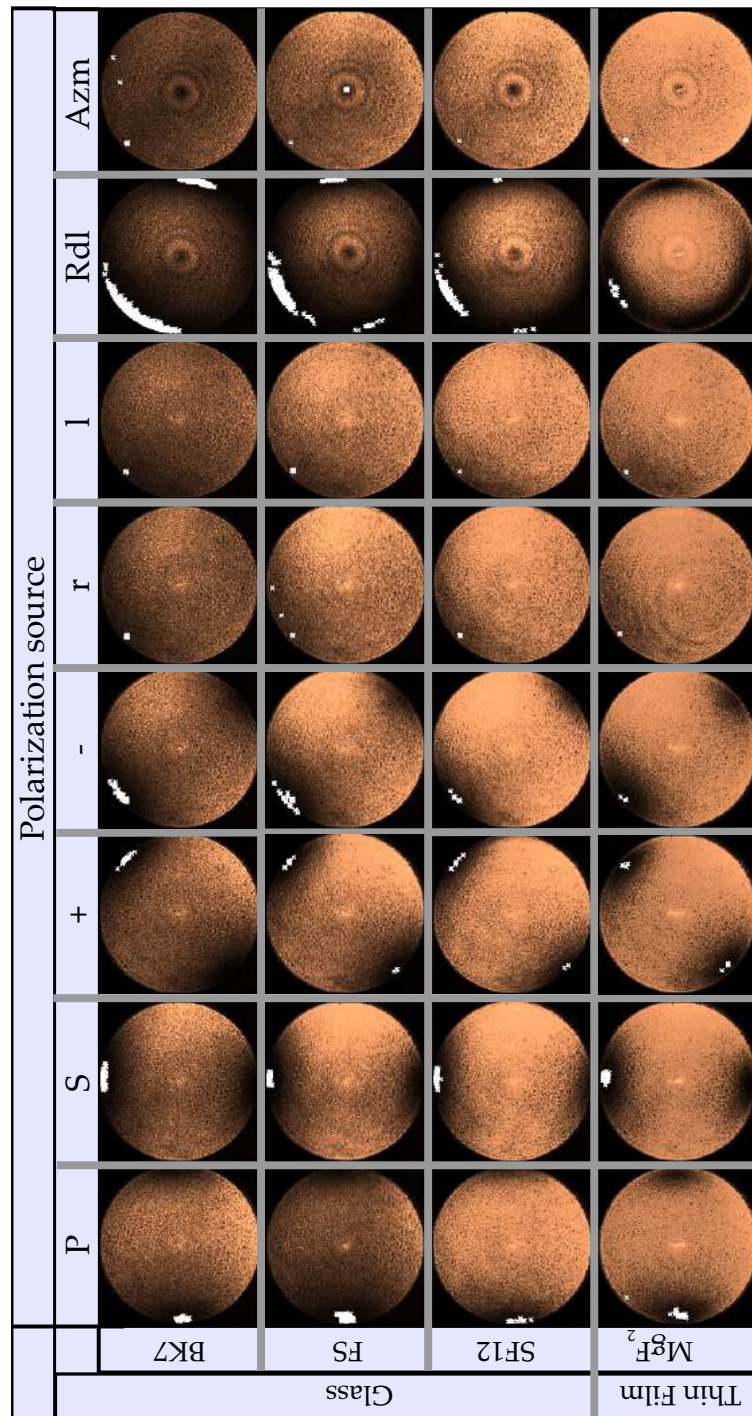


Figure 4.1: Images of experimental results obtained with the microellipsometer at multiple angle-of-incidence. The images were taken at 532 nm. The exposure time was: for BK7: 0.6 ms, for FS and SF12: 1.45 ms, and for MgF_2 : 5ms. The minima obtained, are represented by white marks.

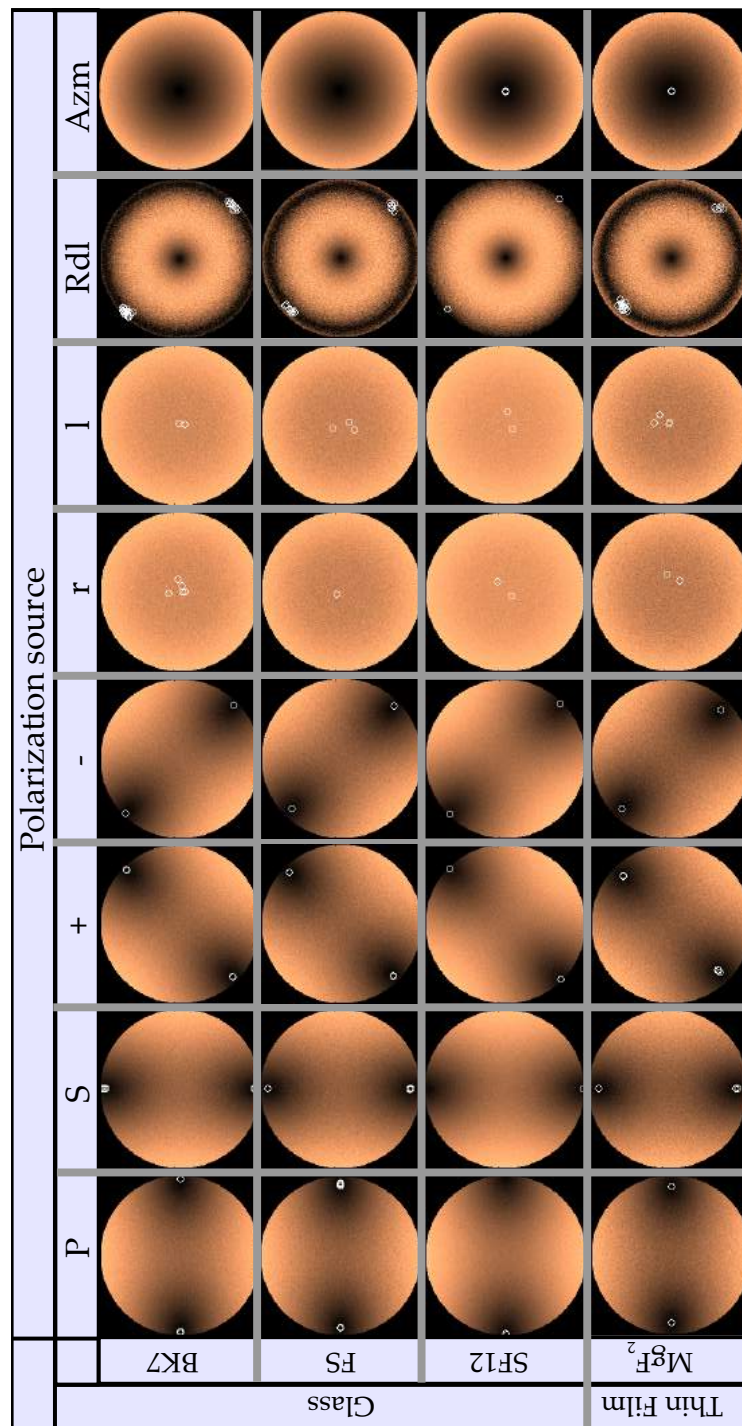


Figure 4.2: Expected images for the samples used. A tolerance of 0.1 for the refractive index value was simulated. The minima obtained, are represented by white circles.

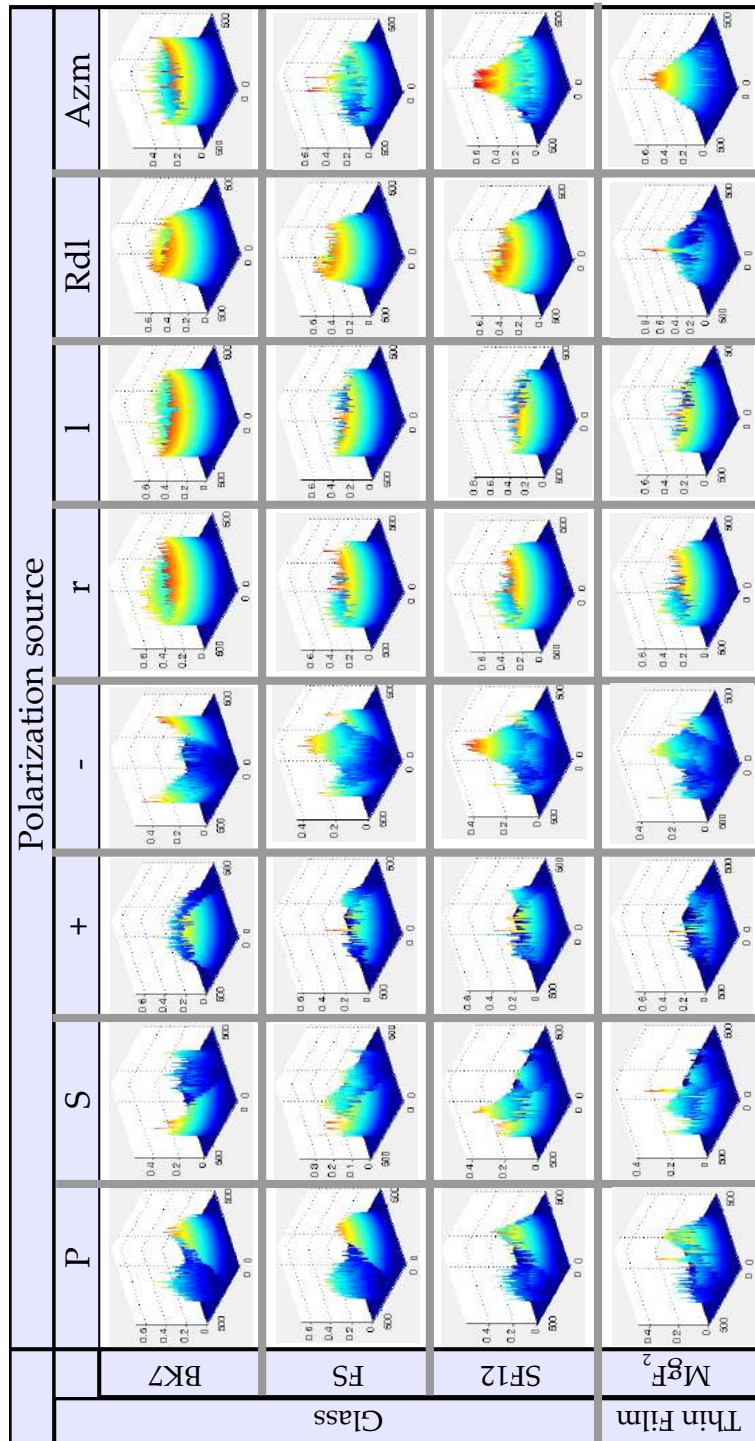


Figure 4.3: Error squared surfaces between the theoretical and experimental images.

		Polarization source									
Class	Sample	Parameter	P	S	+	-	r	l	Rdl	Azm	
		BK7	$\theta_{B,exp}$ error(θ_B) n_{exp} error(n_{exp}) χ^2	56.386° 0.302% 1.504 -1.033% 12976	56.899° 0.118% 1.534 0.921% 11169	57.132° 1.095% 1.548 1.822% 13984	56.220° -1.253% 1.495 -1.651% 12461	55.870° -1.394% 1.475 -2.941% 49090	56.356° -0.536% 1.503 -1.145% 53952	56.752° 0.068% 1.525 0.355% 50904	55.198° -2.579% 1.439 -5.349% 20868
Glass	FS	$\theta_{B,exp}$ error(θ_B) n_{exp} error(n_{exp}) χ^2	56.225° 1.694% 1.495 2.411% 18440	56.868° 3.334% 1.532 4.938% 8897	57.021° 3.557% 1.541 5.555% 11220	57.008° 3.105% 1.540 5.500% 11067	55.713° 0.219% 1.467 0.459% 22534	55.756° 0.296% 1.469 0.616% 23627	55.304° 1.488% 1.500 2.712% 38436	12.273° -77.922% 0.218 -85.099% 13812	
	SF12	$\theta_{B,exp}$ error(θ_B) n_{exp} error(n_{exp}) χ^2	56.988° -3.052% 1.539 -6.721% 11746	56.887° -3.223% 1.539 -7.079% 10166	56.971° -3.081% 1.538 -6.782% 11375	56.259° -4.291% 1.497 -9.267% 13037	55.652° -5.324% 1.463 -11.315% 21990	55.868° -4.957% 1.475 -10.594% 20298	56.778° -3.408% 1.527 -7.461% 43136	55.699° -5.244% 1.496 -9.339% 23805	
Thin Film	MgF ₂	$\theta_{B,exp}$ error(θ_B) n_{exp} error(n_{exp}) χ^2	54.597° 0.607% 1.407 1.223% 9967	55.575° 2.409% 1.459 4.971% 7582	55.263° 1.833% 1.442 3.755% 9094	55.916° 3.036% 1.478 6.324% 9668	56.798° 4.662% 1.528 9.928% 15382	55.904° 3.016% 1.477 6.273% 14468	55.725° 2.686% 1.467 5.561% 13760	55.707° 2.653% 1.466 5.469% 35746	

Figure 4.4: Experimental Brewster's angle and refractive index measured for the samples at each polarization source

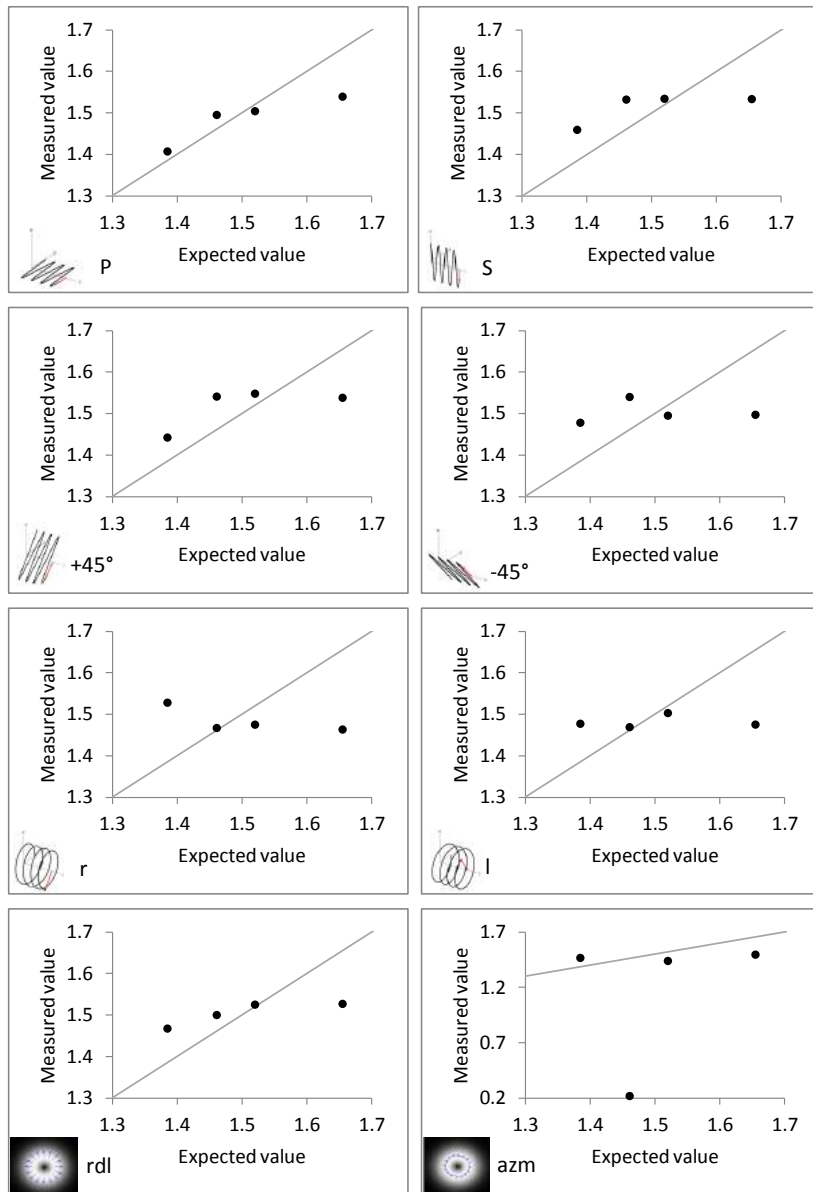


Figure 4.5: Graphs of expected and measured refractive values. The identity curve has been plotted to show which experimental refractive index points, are below or above of the expected value

Sample	Error between expected and measured refractive index values							
	P	S	+	-	R	L	Rdl	Azm
BK7	-0.016	0.014	0.028	-0.025	-0.045	-0.017	0.005	-0.081
FS	0.034	0.071	0.080	0.079	0.006	0.008	0.039	
SF12	-0.116	-0.122	-0.117	-0.158	-0.192	-0.180	-0.128	-0.159
MgF2	0.022	0.074	0.057	0.093	0.143	0.092	0.082	0.081
χ^2	0.015	0.026	0.024	0.040	0.059	0.041	0.025	0.038

Figure 4.6: Error calcs results for each polarization test.

for anisotropic samples, the null zones can lost symmetry. This effect can be quantified by means of the excitation with radial polarization, where the isotropy can be assumed if an exact circle for null zones is drawn.

- The quality of the illumination field and its polarization: although the phenomena could be observed using as illumination source the spot of a laser, the use of beam expander and a spatial filtering to ensure the best homogeneous illumination allow stand out the interested null zones and its distribution better than a laser spot or similar sources where a typical Gaussian profile can be overhead into the interest reflected image. In the case of poor polarization, the effect will be a slight null zones similarly to the images obtained when they are excited with circular polarization.

A careful analysis of the intensity distribution for experimental images, show that although there are symmetry in position of the null zones at north and south poles when the BK7 sample is excited with linear polarization, the null intensities are not equal. That is, one null zone is more near to zero than the other one. This effect is shown in the figure 4.7. For the sample BK7, an intensity difference between the two null zones observed was 50 gray levels¹. This value can be interpreted as a relative intensity difference of 4.88%. For that condition, it is necessary to count 2203 minimum points at the north null zone before to identify the first minimum point at the south null zone. This effect can be interpreted as a metric for the sample's isotropy always that good alignment of the system is guaranteed. Similar conditions was observed for the other samples.

For excitation with radial polarization, an open ring of null zones was observed where a closed was expected in the experimental results. That result can be understood as a systematic error due that for different samples the nulled zones are cutted at the same position. However, later to try with several alignements, they are the best found experimental results.

¹the intensity levels are in the range 0 to 1023.

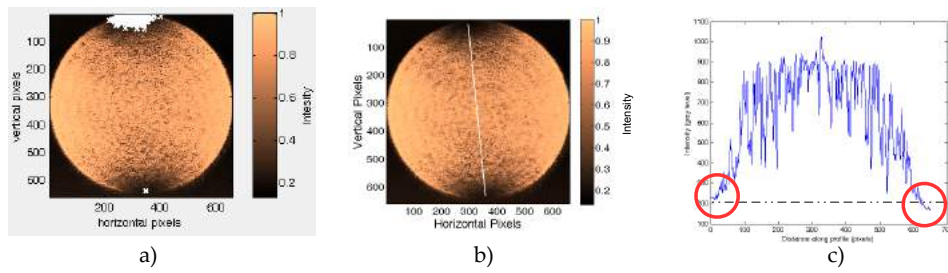


Figure 4.7: Intensity null distribution inside of the condition $\text{Intensity} < \min(\text{Intensity}) + 50$. a) minimum detection given by the computational code. b) Line where the profile analysis is performed. c) intensity profile at the line shown in b).

Chapter 5

Conclusions and perspectives

Zones where the illumination field is extinguished (the named here *null zones*) are relatively easy to watch if an appropriate set of objective lens and samples under study are employed to focus the light beam. For a quick identification of the characteristic Brewster's angle, a long exposure time at the camera should be used. For a carefully sensing of the reflected light distribution, a short exposure time (but long enough to excite the camera sensor) should be employed.

The most complete results to evaluate the refractive index and Brewster's angle, are obtained exciting the sample with radially polarized light. This affirmation is based in the fact that radially polarized light is always into the incidence plane, and testing with this kind of polarization is similar to excite the sample, in a single shot, with linear polarization at all accesible azimuthal orientations, allowing an experiment with multiple repetitions if the sample is isotropic. On the other hand, excitation with azimuthal polarized light does not give relevant information respect to the Brewster's angle and the refractive index. It is due that azimuthal polarized light is always perpendicular to the incidence plane. It explains furthermore the high relative errors at the column AZM of the figure 4.1. In that case, the null zone is identified in a random position, even at the singular point located at the central of the azimuthal polarization source. It can be checked by comparing the experimental and theoretical images (figures 4.1 and 4.2).

Excitation with radially polarized light, has the goodness that allow to get information about the sample's isotropy. A fully symmetric sample will show a circular ring for nulling zones whereas an anisotropic sample should show a non circular ring.

According to the results shown in the table 4.6, excitation with linear polarization states at P , S and $+45^\circ$ orientations, can give as good results

as excitation with radial polarization. In contrast, despite that illumination with circular polarization seems to show low relative errors (figure 4.4), this kind of polarization is not a good illumination source because, although a very weak null ring is expected theoretically 4.2, it does not was observed experimentally. The low relative errors with excitation with circular polarization, occur because the illumination on the experimental image was less intense at the second quadrant of the circle, than in the remaining quadrants. (figure 4.1) and the image processing found the null zones just there. The experimental limitations related with the non-uniformly distributed incident intensities, which were out from our control, generated non-symmetrical images. It explains why the experimental images appear non simmetrical.

The refractive index measurements performed by means of the method shown in this work, is highly sensitive to the image cutting procedure, due that the computational codes assign a field of view (maximum angle) to the squared image size. If a bad cutting is done (that is, if the circle of the illumination does not touch the images limits), the position associated to the null zones is wrong and hence the estimate of the refractive index value.

The matrices strategy to generate synthetic images, proved a suitable tool to make comparisons between expected and measured reflectance fields. Particularly, the use of a refractive index map as an input parameter, spread the simulation to the study of either hypothetical or experimental conditions do not implemented in this work. An example case, could be the study of reflected fields for materials with some specific refractive index's distributions.

The accuracy of the experimental results, depends largely on the camera resolution and the accuracy in refractive index and flatness associated to the calibration sample. With a refractive index deviation less than 5%, the measurement results can be considered right for the purpose of the present work.

According to the experimental results (figure 4.4), is thought that probably the sample SF12, that was supplied by the CIO's optical workshop, is incorrectly labeled. This affirmation is supported by the fact that the excitation with different kind of polarization provided a repetible refractive index value of approximately 1.53 instead of the expected value of 1.65. Another probably reason of the high error between the expected and observed refractive index and Brewster's angle values, is that the SF12 is currently an obsolete Shott glass. It could explains furthermore why the equivalente experimental point at the figure 4.6 is persistently out of the identity line.

As a future work, some tasks could be done to improve the program to generate synthetic images by means of multiple angle-of-incidence microellipsometry. On the one hand, an expansion of the program to generate

unconventional polarization distributions can be done adding another polarization modes. Some examples can be adjust the program for accessing to Hermite-Gauss orders different to H_{01} and H_{10} , allowing theoretical evaluation of reflectance for vortices or spiral polarization modes.

A question that was not answered in this work is the multilayer effect over the reflectance image. In principle, when the objective lens is adjusted to focus the sample's surface, the effect of the transmitted radiation and its contribution for internal reflections (the Bragg's problem) has been neglected and not mentioned because they should introduce noise in a region outside of the angle swept by the objective lens. However, for samples with very low refractive index (for metals for example), this phenomena should be considered.

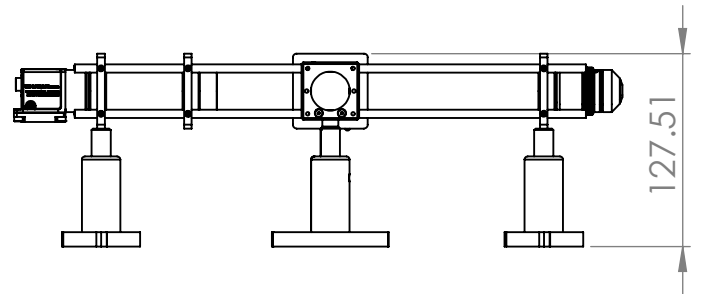
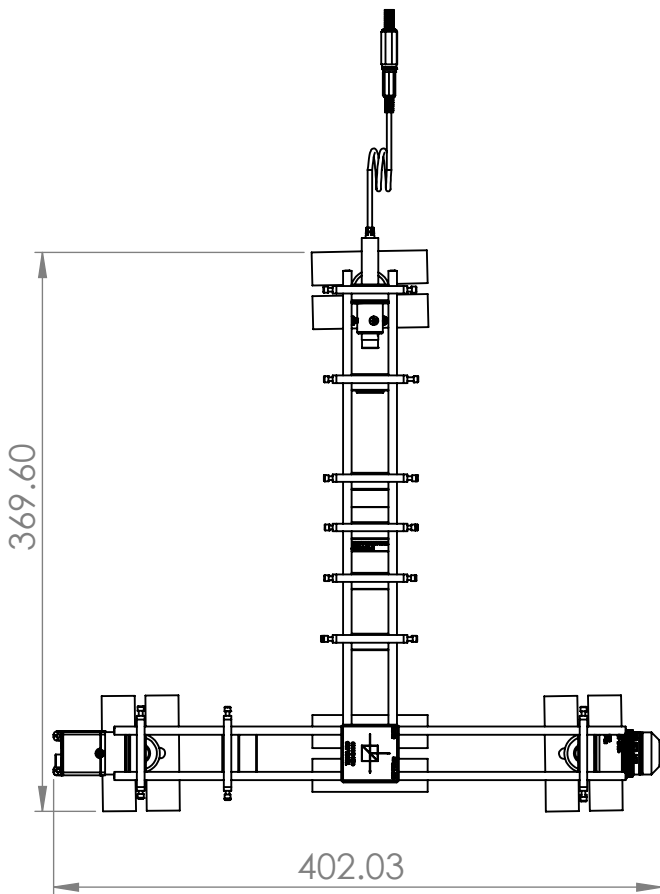
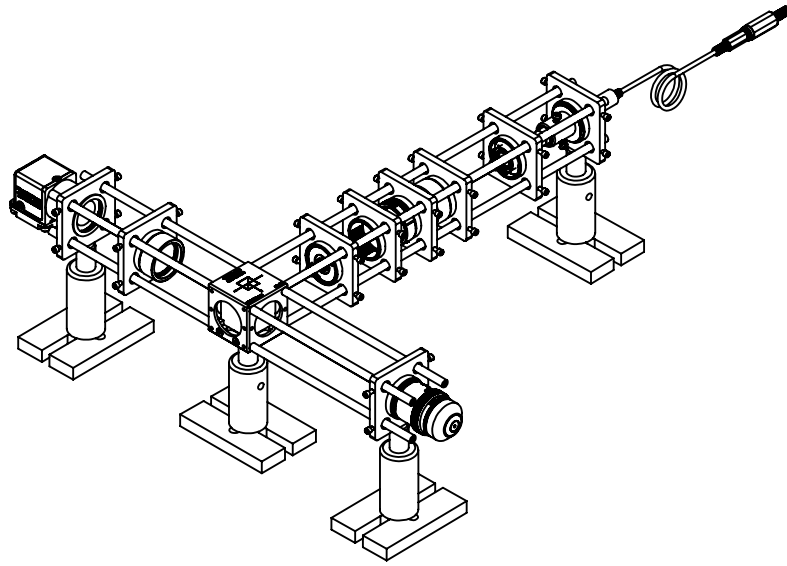
Another question that was not answered is the experimental relationship between the speckle introduced by the surface rugosity and the refractive index tolerance. Theoretically, the amount of speckle can be controlled increasing the tolerance for the refractive index, but experimentally in addition to this parameter, there are speckle contribution originated by the surface rugosity, the optical device's reflection, as well as the speckle contribution of the illumination source.

Chapter 6

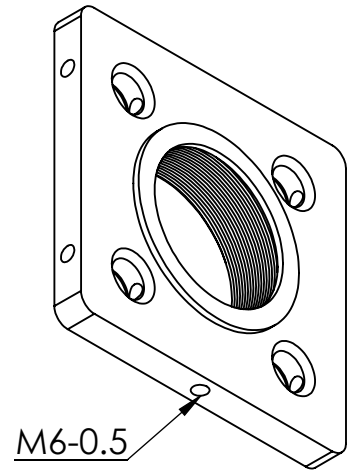
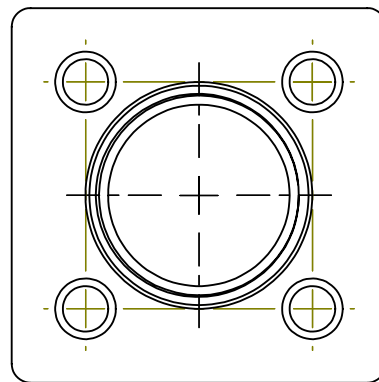
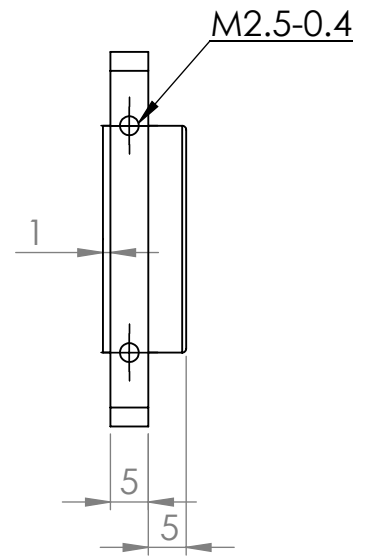
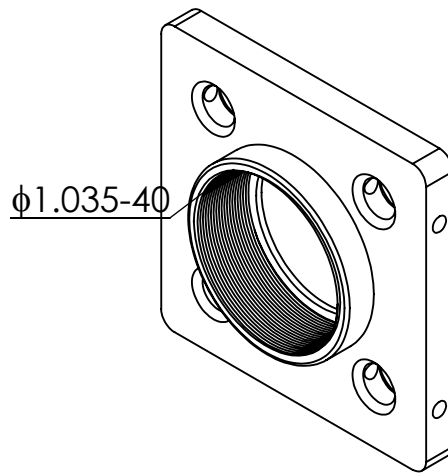
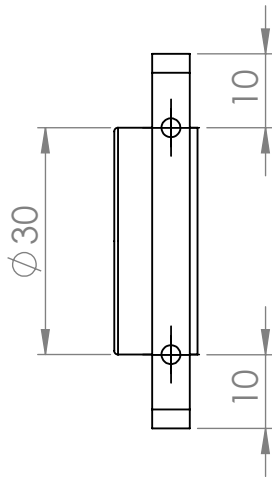
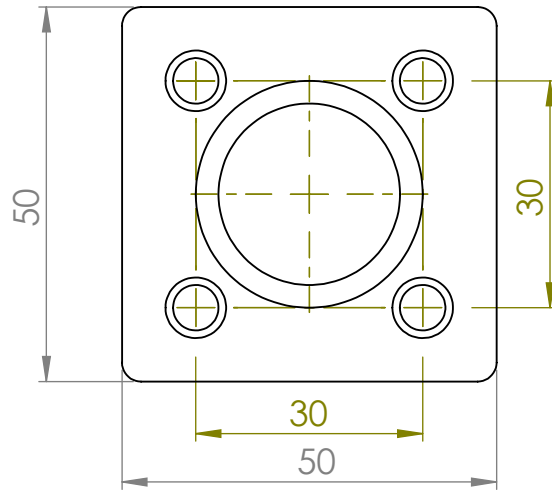
Appendix

6.1 Design of mechanical pieces

As a previous work, a set of mechanical pieces for optical components was designed as initial task. This job was done trying to supply the mechanical needs found before to have the complete experimental setup. These pieces were inspired in the Thorlabs catalog, and its intention is to provide some ideas that can be materialized in a mechanical workshop to reproduce the experimental array presented here. The draws help furthermore to document how the experimental array was finally ensambled.



SI NO SE INDICA LO CONTRARIO: LAS COTAS SE EXPRESAN EN MM ACABADO SUPERFICIAL: TOLERANCIAS: LINEAL: ANGULAR:		ACABADO:		REBARBAR Y ROMPER ARISTAS VIVAS		NO CAMBIE LA ESCALA		REVISIÓN 1.0	
NOMBRE		FIRMA		FECHA		2015-Oct-02		TÍTULO:	
DIBUJ. V. Rico								Microelipsómetro CIO	
VERIF. G. López									
APROB. R. Espinosa								N.º DE DIBUJO	
FABR.									
CALID.				MATERIAL:		Varios Materiales		MicroelipsómetroV1	
				PESO:				ESCALA:1:1	
								HOJA 1 DE 1	
								A4	



SI NO SE INDICA LO CONTRARIO:
LAS COTAS SE EXPRESAN EN MM
ACABADO SUPERFICIAL:
TOLERANCIAS:
LINEAL:
ANGULAR:

REBARBAR Y
ROMPER ARISTAS
VIVAS

NO CAMBIE LA ESCALA

REVISIÓN 2.0

	NOMBRE	FIRMA	FECHA
DIBUJ.	V. Rico		2015-Sep-24
VERIF.	G. López		
APROB.	R. Espinosa		
FABR.			
CALID.			
			MATERIAL: Aluminio
			PESO:

TÍTULO:

Microelipsómetro CIO

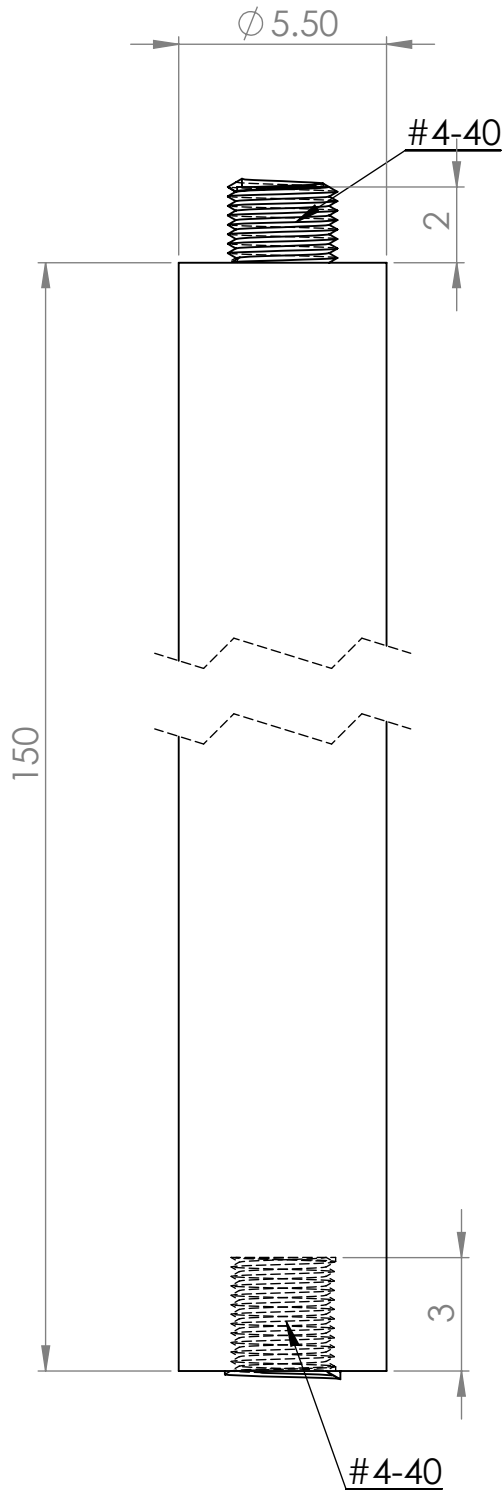
N.º DE DIBUJO

Universal Cage Plate

A4

ESCALA: 1:1

HOJA 1 DE 1



SI NO SE INDICA LO CONTRARIO:
LAS COTAS SE EXPRESAN EN MM
ACABADO SUPERFICIAL:
TOLERANCIAS:
LINEAL:
ANGULAR:

ACABADO:

REBARBAR Y
ROMPER ARISTAS
VIVAS

NO CAMBIE LA ESCALA

REVISIÓN 1.0

NOMBRE	FIRMA	FECHA	2015-Sep-24
DIBUJ. V. Rico			
VERIF. G. López			
APROB. R. Espinosa			
FABR.			
CALID.			
MATERIAL:			
Aluminio			
PESO:			

TÍTULO:

Microelipsómetro CIO

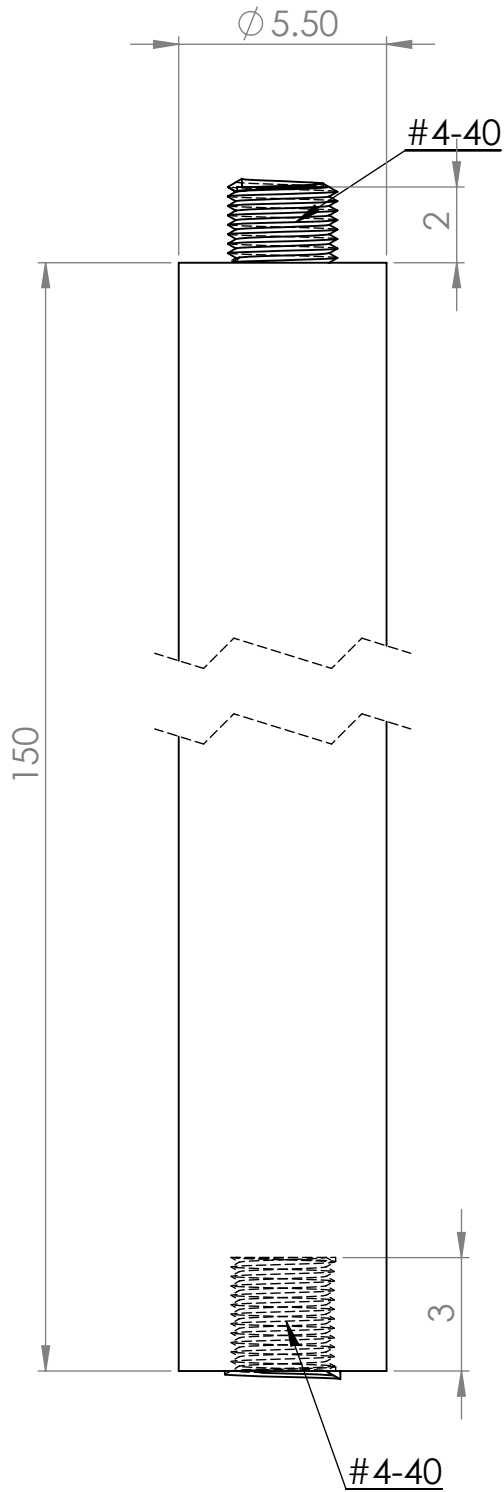
N.º DE DIBUJO

Eje 150mm

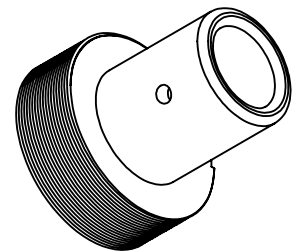
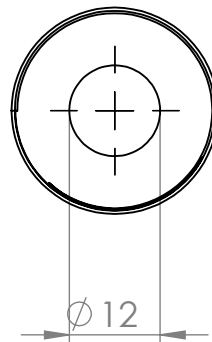
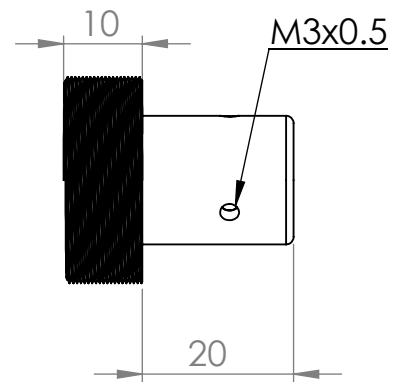
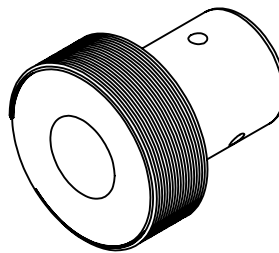
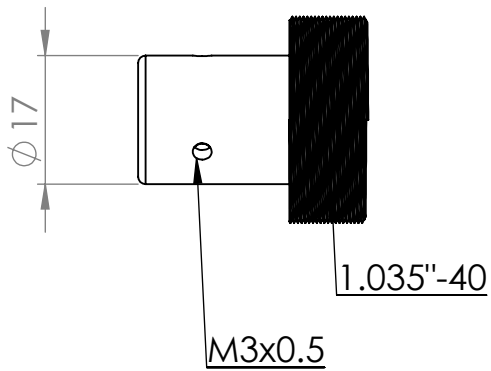
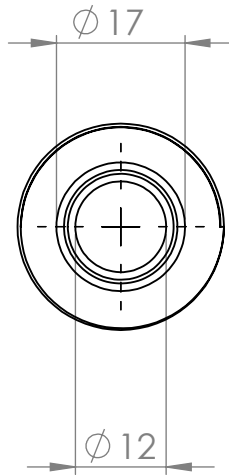
A4

ESCALA:1:1

HOJA 1 DE 1



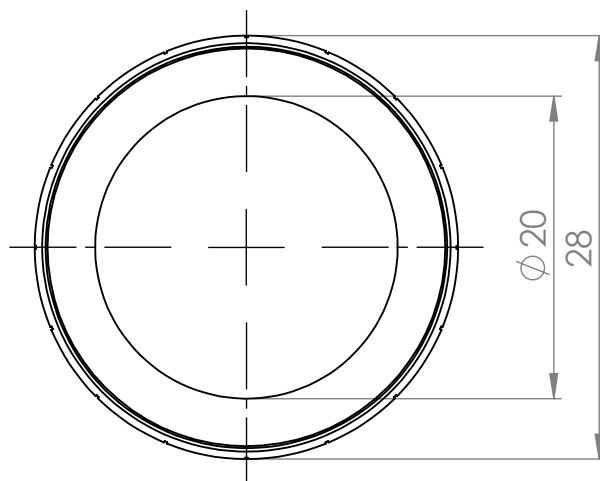
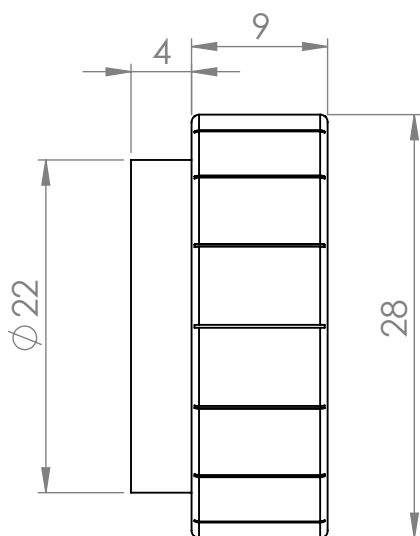
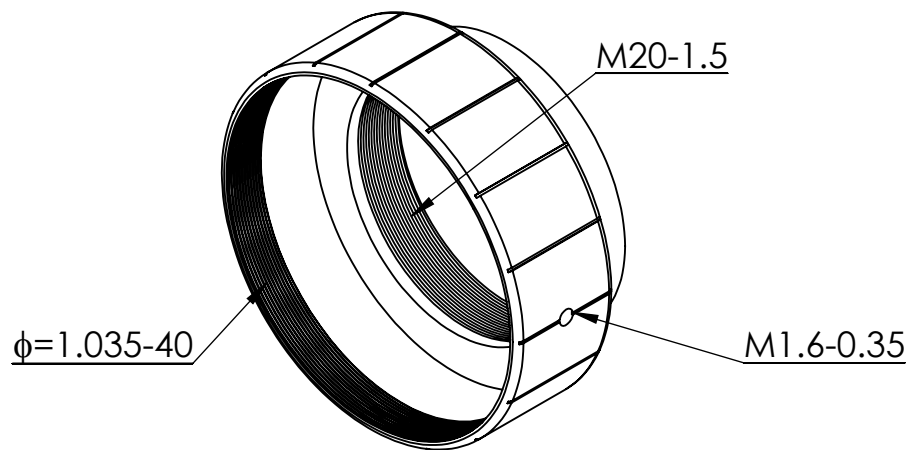
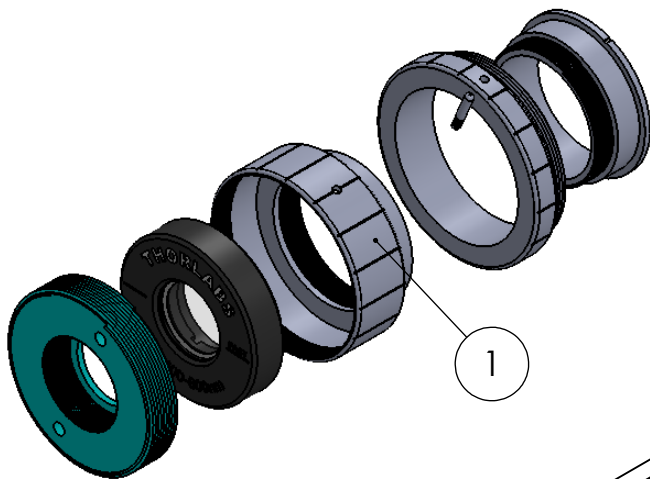
SI NO SE INDICA LO CONTRARIO: LAS COTAS SE EXPRESAN EN MM ACABADO SUPERFICIAL: TOLERANCIAS: LINEAL: ANGULAR:		ACABADO:		REBARBAR Y ROMPER ARISTAS VIVAS		NO CAMBIE LA ESCALA		REVISIÓN 1.0	
NOMBRE		FIRMA		FECHA		2015-Sep-24		TÍTULO:	
DIBUJ. V. Rico								Microelipsómetro CIO	
VERIF. G. López									
APROB. R. Espinosa									
FABR.									
CALID.				MATERIAL:		N.º DE DIBUJO		Eje 150mm	
				Aluminio				A4	
				PESO:		ESCALA:1:1		HOJA 1 DE 1	



SI NO SE INDICA LO CONTRARIO: LAS COTAS SE EXPRESAN EN MM ACABADO SUPERFICIAL: TOLERANCIAS: LINEAL: ANGULAR:			ACABADO:			REBARBAR Y ROMPER ARISTAS VIVAS		NO CAMBIE LA ESCALA		REVISIÓN 2.0	
NOMBRE			FIRMA			FECHA			2015-Sep-24		
DIBUJ.			V. Rico			VERIF.			G. López		
APROB.			R. Espinosa			FABR.					
CALID.						MATERIAL:			Aluminio		
PESO:						N.º DE DIBUJO			Acople Laser		
ESCALA: 1:1						HOJA 1 DE 1			A4		

TÍTULO:
Microelipsómetro CIO

Acople Laser



SI NO SE INDICA LO CONTRARIO:
 LAS COTAS SE EXPRESAN EN MM
 ACABADO SUPERFICIAL:
 TOLERANCIAS:
 LINEAL:
 ANGULAR:

ACABADO:

REBARBAR Y
 ROMPER ARISTAS
 VIVAS

NO CAMBIE LA ESCALA

REVISIÓN 1.0

NOMBRE	FIRMA	FECHA	2015-Oct-26
DIBUJ. V. Rico			
VERIF. G. López			
APROB. R. Espinosa			
FABR.			
CALID.			
MATERIAL:		Aluminio	
PESO:			

TÍTULO:

Microelipsómetro CIO

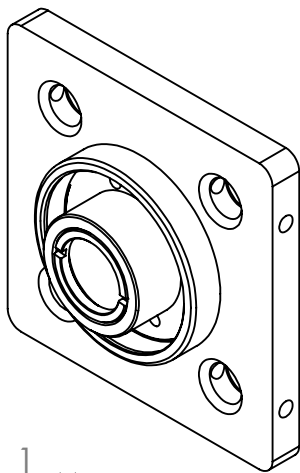
N.º DE DIBUJO

Acople Retardador

A4

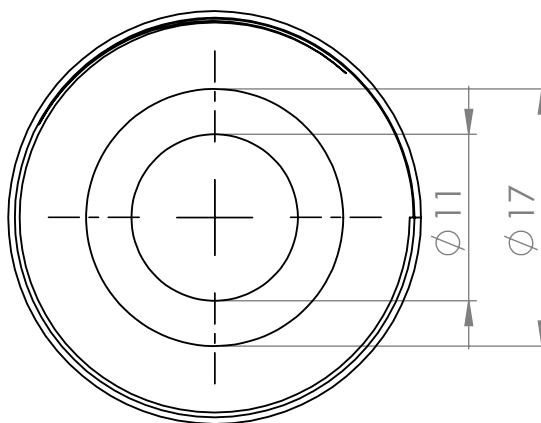
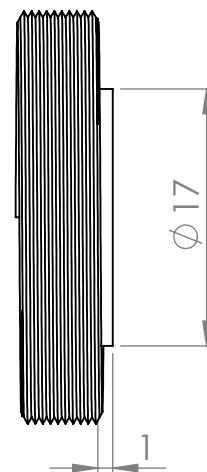
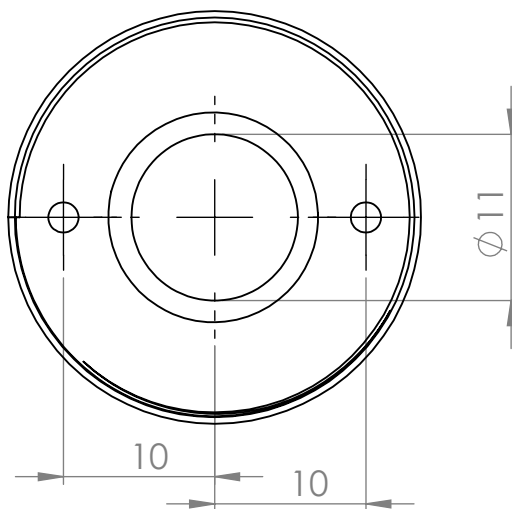
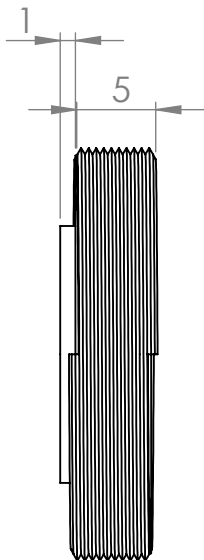
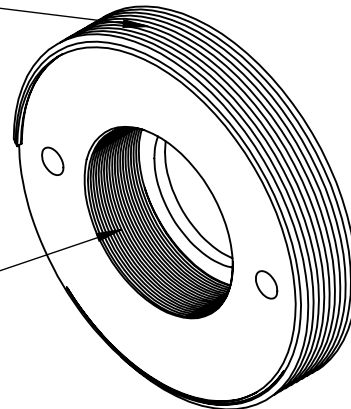
ESCALA:2:1

HOJA 1 DE 1



$\phi=1.035''-40$

$\phi=0.535''-40$



SI NO SE INDICA LO CONTRARIO:
LAS COTAS SE EXPRESAN EN MM
ACABADO SUPERFICIAL:
TOLERANCIAS:
LINEAL:
ANGULAR:

ACABADO:

REBARBAR Y
ROMPER ARISTAS
VIVAS

NO CAMBIE LA ESCALA

REVISIÓN 1.0

	NOMBRE	FIRMA	FECHA	
DIBUJ.	V. Rico		2015-Sep-30th	
VERIF.	G. López			
APROB.	R. Espinosa			
FABR.				
CALID.				MATERIAL: Aluminio
				PESO:

TÍTULO:

Microelipsómetro CIO

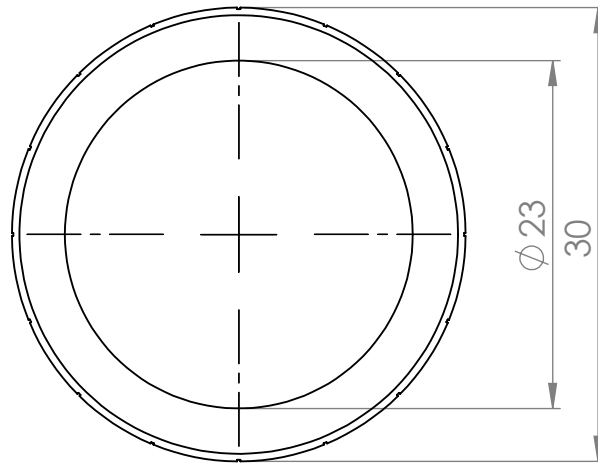
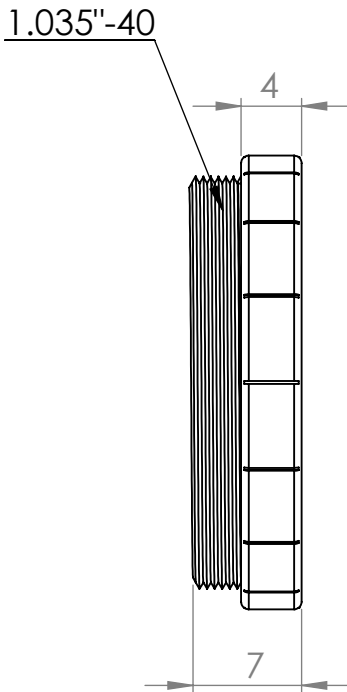
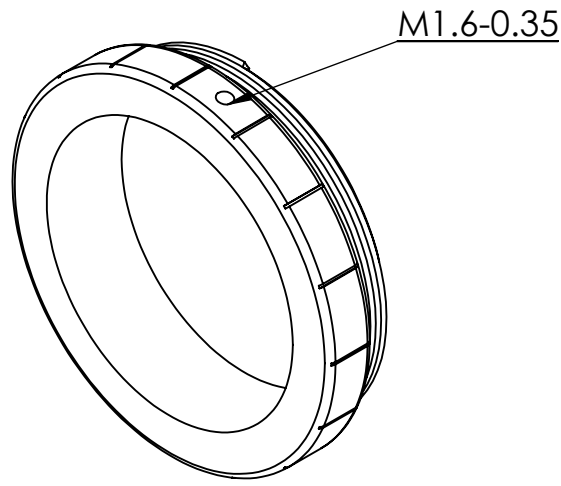
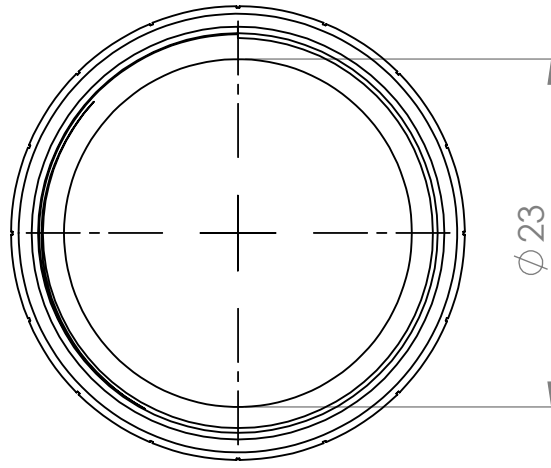
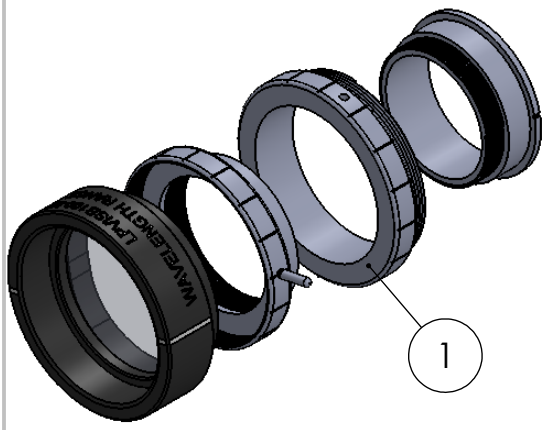
N.º DE DIBUJO

AcopleSM05L03

A4

ESCALA:2:1

HOJA 1 DE 1



SI NO SE INDICA LO CONTRARIO:
LAS COTAS SE EXPRESAN EN MM
ACABADO SUPERFICIAL:
TOLERANCIAS:
LINEAL:
ANGULAR:

ACABADO:

REBARBAR Y
ROMPER ARISTAS
VIVAS

NO CAMBIE LA ESCALA

REVISIÓN 1.0

	NOMBRE	FIRMA	FECHA	2015-Oct-13
DIBUJ.	V. Rico			
VERIF.	G. López			
APROB.	R. Espinosa			
FABR.				
CALID.				
			MATERIAL:	
			Aluminio	
			PESO:	

TÍTULO:

Microelipsómetro CIO

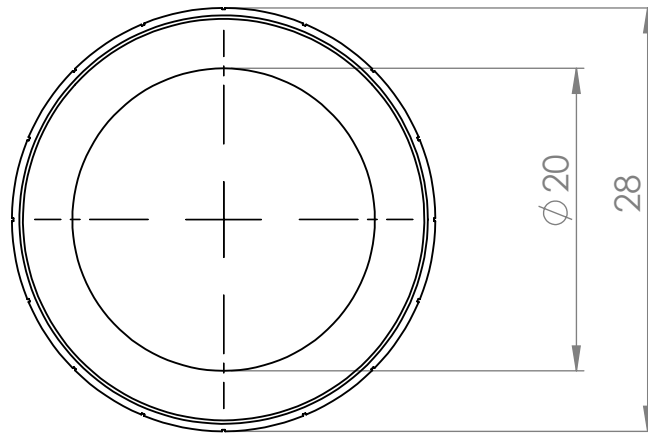
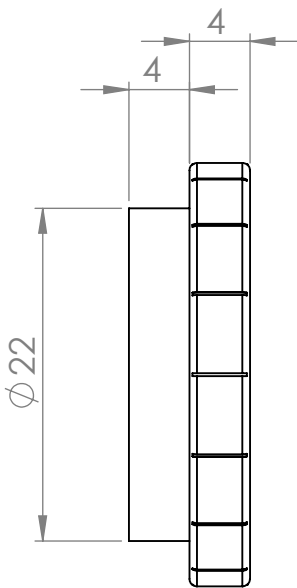
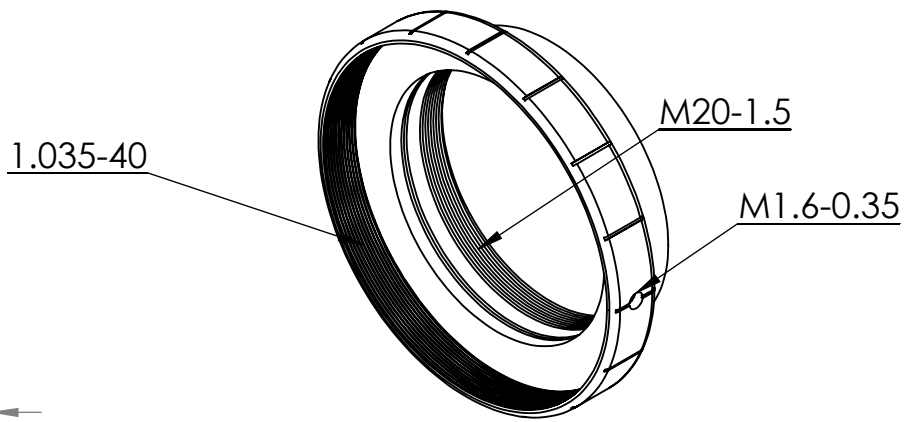
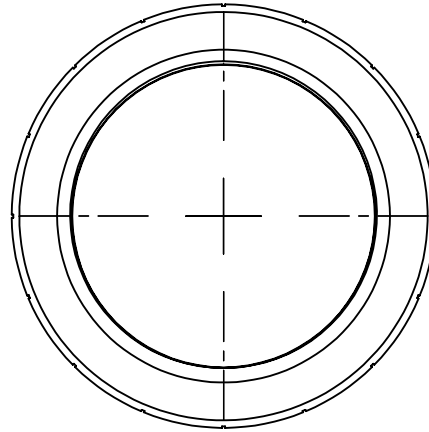
N.º DE DIBUJO

Acople Polarizador Pieza 1

A4

ESCALA:2:1

HOJA 1 DE 1



SI NO SE INDICA LO CONTRARIO:
 LAS COTAS SE EXPRESAN EN MM
 ACABADO SUPERFICIAL:
 TOLERANCIAS:
 LINEAL:
 ANGULAR:

ACABADO:

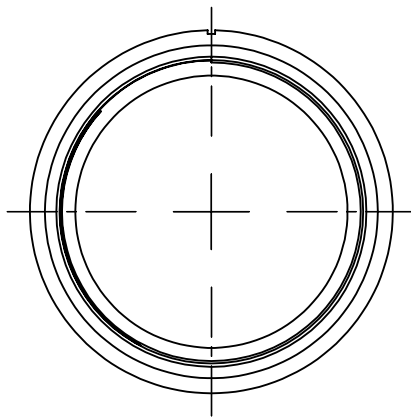
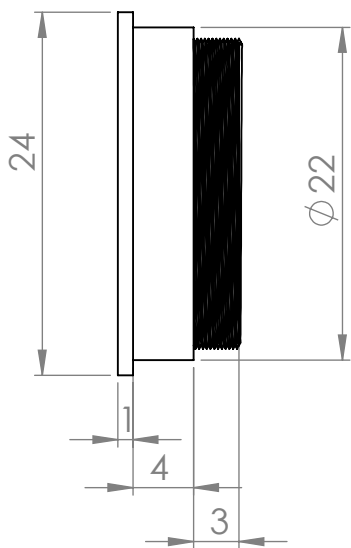
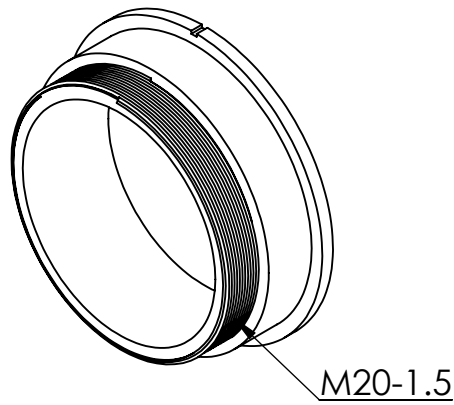
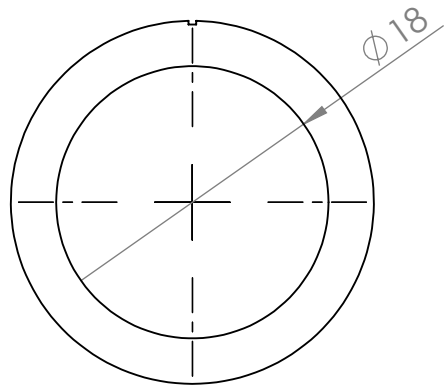
REBARBAR Y
 ROMPER ARISTAS
 VIVAS

NO CAMBIE LA ESCALA

REVISIÓN 1.0

NOMBRE	FIRMA	FECHA	2015-Oct-13
DIBUJ. V. Rico			
VERIF. G. López			
APROB. R. Espinosa			
FABR.			
CALID.			
MATERIAL: Aluminio		PESO:	

TÍTULO: Microelipsómetro CIO	
N.º DE DIBUJO Acople PolarizadorPieza2	A4
ESCALA:2:1	HOJA 1 DE 1



SI NO SE INDICA LO CONTRARIO:
LAS COTAS SE EXPRESAN EN MM
ACABADO SUPERFICIAL:
TOLERANCIAS:
LINEAL:
ANGULAR:

ACABADO:

REBARBAR Y
ROMPER ARISTAS
VIVAS

NO CAMBIE LA ESCALA

REVISIÓN 1.0

	NOMBRE	FIRMA	FECHA	2015-Oct-13
DIBUJ.	V. Rico			
VERIF.	G. López			
APROB.	R. Espinosa			
FABR.				
CALID.				
			MATERIAL:	
			Aluminio	
			PESO:	

TÍTULO:

Microelipsómetro CIO

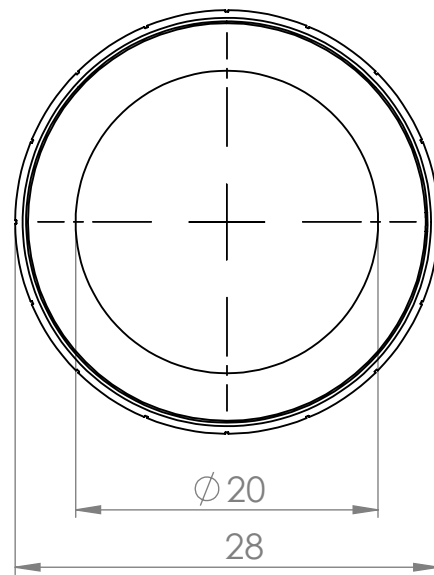
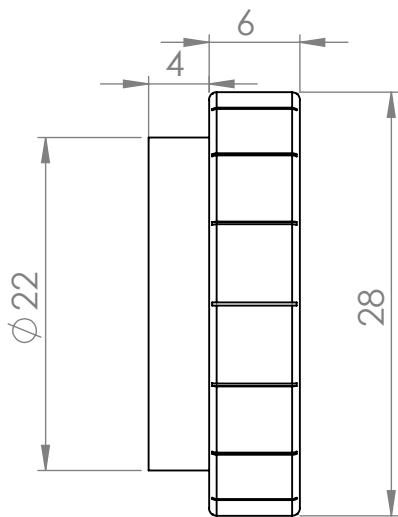
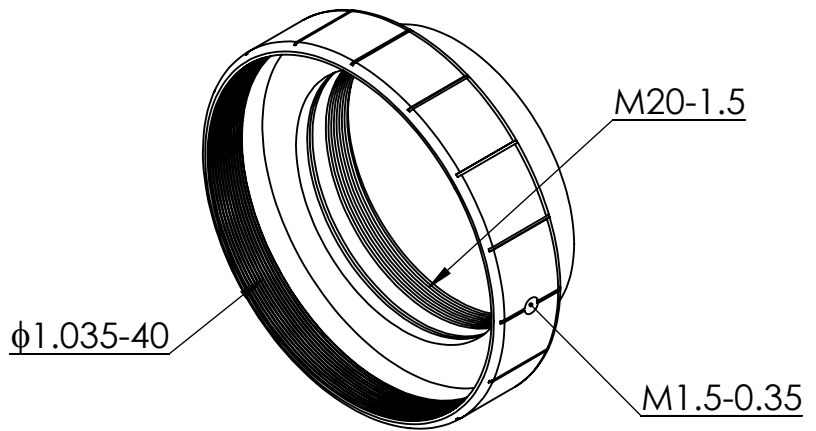
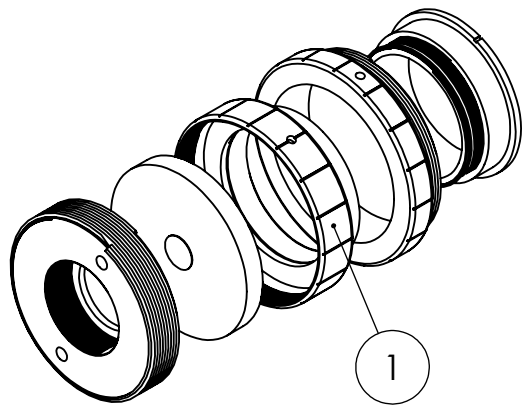
N.º DE DIBUJO

Acople PolarizadorPieza3

A4

ESCALA:2:1

HOJA 1 DE 1



SI NO SE INDICA LO CONTRARIO:
LAS COTAS SE EXPRESAN EN MM
ACABADO SUPERFICIAL:
TOLERANCIAS:
LINEAL:
ANGULAR:

ACABADO:

REBARBAR Y
ROMPER ARISTAS
VIVAS

NO CAMBIE LA ESCALA

REVISIÓN 1.0

	NOMBRE	FIRMA	FECHA
DIBUJ.	V. Rico		2015-Oct-23
VERIF.	G. López		
APROB.	R. Espinosa		
FABR.			
CALID.			

MATERIAL:
Aluminio

PESO:

TÍTULO:

Microelipsómetro CIO

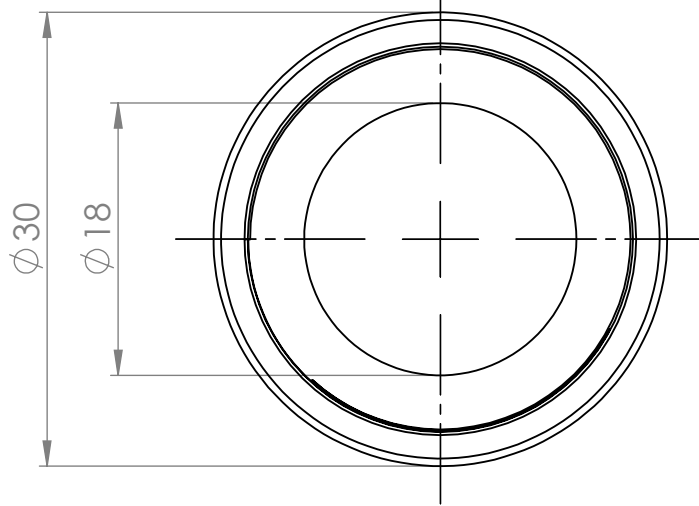
N.º DE DIBUJO

AcopleSWaveplate

A4

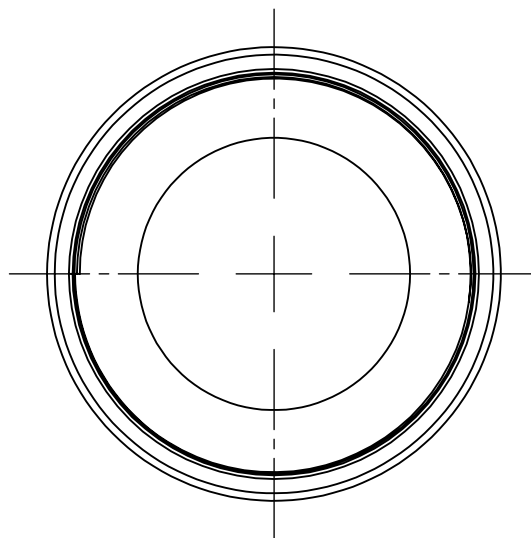
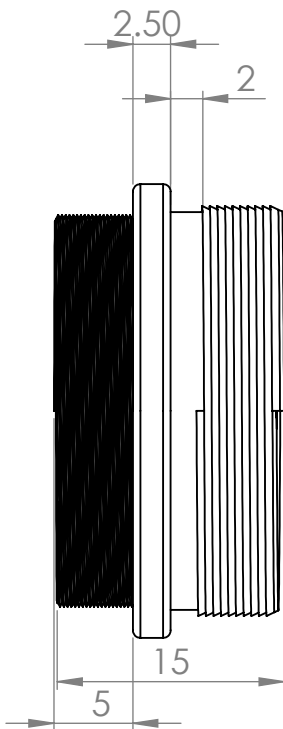
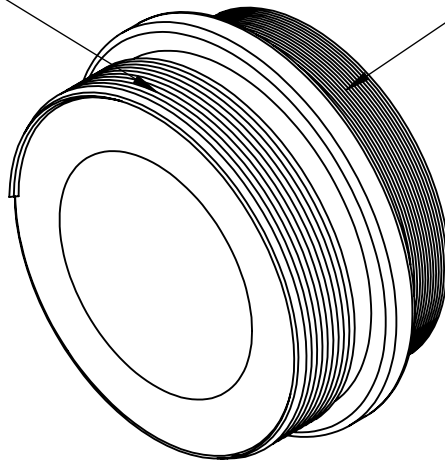
ESCALA:2:1

HOJA 1 DE 1



#1.035-40

#1-32



SI NO SE INDICA LO CONTRARIO:
LAS COTAS SE EXPRESAN EN MM
ACABADO SUPERFICIAL:
TOLERANCIAS:
LINEAL:
ANGULAR:

ACABADO:

REBARBAR Y
ROMPER ARISTAS
VIVAS

NO CAMBIE LA ESCALA

REVISIÓN 1.0

NOMBRE	FIRMA	FECHA	2015-Oct-02
DIBUJ. V. Rico			
VERIF. G. López			
APROB. R. Espinosa			
FABR.			
CALID.			
MATERIAL: Aluminio		PESO:	

TÍTULO:

Microelipsómetro CIO

N.º DE DIBUJO

Acople Cámara

A4

ESCALA:1:1

HOJA 1 DE 1

6.3 MatLAB code for reflectanceAtMAI.m

```

1  % REFLECTANCEATMAI Reflectance at multiple angle-of-incidence
2  %                               for any polarization field.
3  %                               by: Victor-Manuel Rico-Botero
4  %                               May 01, 2016
5  %
6  % Calculate the reflectance image for a given polarization
7  % field, using the Jones formulism.
8  % E_x : horizontal Jones component for the incident electric field
9  % E_y : vertical Jones component for the incident electric field
10 % delta: retardance between horizontal and vertical electric fields
11 % polType: 'conv' for conventional polarization; 'unconv' for
12 % unconventional polarization modes
13 % n_s: Average refractive index for the sample
14 % NA: Numerical aperture for the objective lens
15 % tol: tolerance around the central refractive index value
16 %
17 % example: [Ex,Ey]=reflectanceAtMAI(1,1,0,'unconv',1.6,0.7,0.1);

18 function [Ep_r,Es_r]=reflectanceAtMAI(E_x,E_y,delta,...
19                                     polType,n_s,NA,tol)
20 rho=300;
21 thetaMax=asin(NA);
22 f=rho/tan(thetaMax);
23 pixelsVector=linspace(-rho,rho,2*rho);
24 [x,y]=meshgrid(pixelsVector);
25 r=sqrt(x.^2+y.^2);
26 cuadrantI=(x>=0)&(y>=0);
27 cuadrantII=(x<0)&(y>=0);
28 cuadrantIII=(x<0)&(y<0);
29 cuadrantIV=(x>=0)&(y<0);
30 phyI=atan(y./x).*cuadrantI;
31 phyII=(atan(y./x)+pi).*cuadrantII;
32 phyIII=(atan(y./x)+pi).*cuadrantIII;
33 phyIV=(atan(y./x)+2*pi).*cuadrantIV;
34 phy=phyI+phyII+phyIII+phyIV;
35 switch polType
36     case 'conv'
37         Ex=E_x*ones(length(x),length(y))*exp(1i*delta);
38         Ey=E_y*ones(length(x),length(y));
39     case 'unconv'
40         [Ex,Ey]=rAndAV2('r',632E-9,12,0,1.6);

```

```
41 end
42 ExPositive=Ex>0;
43 ExNegative=Ex<0;
44 EyPositive=Ey>0;
45 EyNegative=Ey<0;
46 alphaI=atan(Ey./Ex).*ExPositive.*EyPositive;
47 alphaII=(atan(Ey./Ex)+pi).*ExNegative.*EyPositive;
48 alphaIII=(atan(Ey./Ex)+pi).*ExNegative.*EyNegative;
49 alphaIV=(atan(Ey./Ex)+2*pi).*ExPositive.*EyNegative;
50 alpha=alphaI+alphaII+alphaIII+alphaIV;
51 alpha=alpha';
52 E=sqrt(Ex.*conj(Ex)+Ey.*conj(Ey));
53 Ep_i=E.*cos((phy-alpha));
54 Es_i=sqrt((E.*cos(alpha)-Ep_i.*cos(phy)).^2+...
55           (E.*sin(alpha)-Ep_i.*sin(phy)).^2);
56 theta_i=atan(r/f); % incidence angle
57 n=n_s*ones(size(theta_i)); % Refractive index map
58 n=n+tol*rand(size(theta_i))-tol*rand(size(theta_i));
59 theta_t=asin(1./n.*sin(theta_i));
60 r_p=(tan(theta_i-theta_t)./tan(theta_i+theta_t));
61 r_s=-(sin(theta_i-theta_t)./sin(theta_i+theta_t));
62 r_p(isnan(r_p))=((n(1)-1)/(n(1)+1));
63 r_s(isnan(r_s))=((n(1)-1)/(n(1)+1));
64 Ep_r=r_p.*Ep_i;
65 Es_r=r_s.*Es_i;
```

6.4 MatLAB code for rAndAV2.m

```

1  % RANDAV2 generates radial and azimuthal distribution matrices.
2  %                               by, Victor-Manuel Rico-Botero
3  %                               2016-Apr-28th
4  % lambda: wavelenght
5  % w0: width of the beam waist
6  % z: beam position at the propagation axis
7  % E0: field amplitude
8  % example: [Ex,Ey]=rAndAV2('r',632E-9,6,0,1.6)
9
10 function [Ex,Ey]=rAndAV2(polType,lambda,w0,z,E0)
11 rho=300;
12 pixelsVector=linspace(-1,1,2*rho);
13 [x,y]=meshgrid(pixelsVector*2E7*lambda);
14 k=2*pi/lambda;
15 z0=(k*w0^2)/2;
16 wz=w0*sqrt(1+(z/z0)^2);
17 qz=z+1i*z0;
18 m=0;
19 n=1;
20 phy=(1+m+n)*atan(z/z0);
21 h0=1;
22 h1_y=2*sqrt(2)*y/wz;
23 h1_x=2*sqrt(2)*x/wz;
24 % -----Modes calculation-----
25 E01=E0*w0/wz*h1_y.*exp(-1i*phy).*exp(-(x.^2+y.^2)*k/(2*qz));
26 E10=E0*w0/wz*h1_x.*exp(-1i*phy).*exp(-(x.^2+y.^2)*k/(2*qz));
27 switch polType
28     case 'r'
29         Ex=E01;
30         Ey=E10;
31     case 'a'
32         Ex=-E10;
33         Ey=E01;
34 end

```

6.5 MatLab code for findMinimum2.m

```
1 % FINDMINIMUM2 find the coordinates for the absolute minimum
2 %           values at multiple angle-of-incidence
3 %           microellipsometry of synthetic images.
4 %           By, Victor-Manuel Rico-Botero
5 %           2015-dec-28th
6 %
7 % A: synthetic monochromatic and squared matrix image
8 % imageDiameter: diameter of the interest area
9 %
10 % Execution example: [ix,iy]=findMinimum2(A,300)
11
12 function [ix,iy]=findMinimum2(A,imageDiameter)
13 rho=imageDiameter/2;
14 pixelsVector=linspace(-rho,rho,imageDiameter);
15 [x,y]=meshgrid(pixelsVector);
16 r=sqrt(x.^2+y.^2);
17 minValue=min(min(A(r<rho)));
18 idx=find(A==minValue);
19 [ix,iy]=ind2sub(size(A),idx);
```

6.6 MatLab code for findMinimumExp.m

```
1 % FINDMINIMUMEXP found the coordinates for the absolute minimum
2 %           values at multiple angle-of-incidence
3 %           microellipsometry of experimental images.
4 %           By, Victor-Manuel Rico-Botero
5 %           2016-Apr-02nd
6 %
7 % A: synthetic monochromatic and squared matrix image
8 % imageDiameter: diameter of the interest area
9 % epsilon: tolerance in the absolute minimum value
10 %
11 % Execution example: [ix,iy]=findMinimum2(A,300,10)
12
13 function [ix,iy]=findMinimumExp(A,imageDiameter,epsilon)
14 rho=imageDiameter/2;
15 pixelsVector=linspace(-rho,rho,imageDiameter);
16 [x,y]=meshgrid(pixelsVector);
17 r=sqrt(x.^2+y.^2);
18 minValue=min(min(A(r<rho)));
19 lowerLimit=(r<rho)& image>=minValue;
20 upperLimit=(r<rho)& image<(minValue+epsilon);
21 idx=find(lowerLimit & upperLimit);
22 [ix,iy]=ind2sub(size(A),idx);
```

6.7 Technical problems and solutions

The process of image recording in the implementation of the microellipsometer of multiple angle-of-incidence, can show some technical problems that were solved in this work. Particularly the image saturation, generated by the use of a laser source, usually saturates the camera and good image for processing can be hard to obtain. It was solved by means of two methods:

- Attenuating the illumination field with a set of neutral density filters. This filters were located between the output of the laser source and the beginning of the optical setup.
- Controlling the time exposition at the camera sensor.

On the other hand, the first setup idea was to illuminate the sample using only the laser spot as light source, but then expanding that beam and performing it through a spatial filter, allowed to control the illumination homogeneity directly on the sample when a conventional polarization is used, and before to the s-waveplate when a non-conventional polarization experiments was done.

Another problem is that using a non polarizing beam splitter (NPBS) to redirect the illumination field from the PSG to objective lens, makes interference fringes in the image recorded by the camera sensor, and that fringes are an undesirable effect for the purpose that is followed in this work. To solve that, a slight misalignment of the NPBS can be performed splitting the interest image of the interference fringes for some axial camera's position. The problem of the interference fringes is show at figure 6.1. Another way to remove the interference fringe, is by means of digital spatial filtering; it can be developed performing a Fourier transform to the experimental image, removing the spatial frequencies corresponding to interference fringes and performing an inverse Fourier transform to retrieve the experimental image but without the interference fringes. This procedure was executed but further to remove fringes, interest information was losted too. Finally, fringes removed by NPBS misalignment was convincing for the authors.

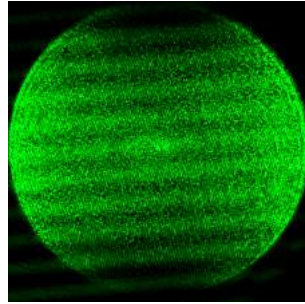


Figure 6.1: Undesirable interference fringes seen by the camera when a geometrical alignment of the NPBS is done.

Bibliography

- [1] R.M.A. Azzam and N.M. Bashara. *Ellipsometry and polarized light*. North-Holland personal library. North-Holland Pub. Co., 1977.
- [2] V V Barun and A P Ivanov. Light scattering by a rough surface of human skin. 1. the luminance factor of reflected light. *Quantum Electronics*, 43(8):768, (2013).
- [3] W.W. Bell. *Special Functions for Scientists and Engineers*. Dover books on mathematics. Dover Publications, (2004).
- [4] M. Beresna, M. Gecevicius, P. Kazansky, and T. Gertus. Radially polarized optical vortex converter created by femtosecond laser nanostructuring of glass. *Appl. Phys. Lett.*, 98:201101, (2011).
- [5] D. Bouhafs, A. Moussi, A. Chikouche, and J.M. Ruiz. Design and simulation of antireflection coating systems for optoelectronic devices: Application to silicon solar cells. *Solar Energy Materials and Solar Cells*, 52(12):79 – 93, (1998).
- [6] E. Collett. *Field Guide to Polarization*. Field Guide Series. The International Society for Optics and Photonics, (2005).
- [7] R E Denton, R D Campbell, and S G Tomlin. The determination of the optical constants of thin films from measurements of reflectance and transmittance at normal incidence. *Journal of Physics D: Applied Physics*, 5(4):852, (1972).
- [8] R. Espinosa-Luna and Q. Zhan. Polarization and polarizing optical devices. In D. Malacara and J. Thompson, editors, *Handbook of Optical Engineering*. Taylor and Francis, (2015).
- [9] D.H. Goldstein. *Polarized Light, Third Edition*. CRC Press, (2010).
- [10] J.C. Granada. *Teoría Electromagnética*. Programa editorial de la Universidad del Valle, (2012).

-
- [11] Olympus Inc. Pupil diameter and beam spot diameter of objective lens. http://www.olympus-ims.com/es/microscope/terms/luminous_flux/, (2016).
- [12] Shott Inc. Optical glass datasheets. <http://refractiveindex.info/download/data/2015/schott-optical-glass-collection-datasheets-july-2015-us.pdf>, (2015).
- [13] T. Jenkins. Multiple-angle-of-incidence ellipsometry. *Appl. Phys.*, **32**:R45–R56, (1999).
- [14] Shui-Yang Lien, Dong-Sing Wu, Wen-Chang Yeh, and Jun-Chin Liu. Tri-layer antireflection coatings (sio2/sio2tio2/tio2) for silicon solar cells using a solgel technique. *Solar Energy Materials and Solar Cells*, 90(16):2710 – 2719, (2006).
- [15] I. H. Malitson. Interspecimen comparison of the refractive index of fused silica. *J. Opt. Soc. Am.*, 55:1205–1209, (1965).
- [16] J.F. Murray-Coleman and A.M. Smith. The automated measurement of brdfs and their application to luminaire modeling. *Journal of the Illuminating Engineering Society*, pages 87–99, (1990).
- [17] National Institute of Standards and Technology. Spectral tri-function automated reference reflectometer. http://www.nist.gov/pml/div685/grp03/spectrophotometry_starr.cfm, (2016).
- [18] E. D. Palik. *Handbook of Optical Constants of Solids II*. Academic Press handbook series. Academic Press, 1991.
- [19] Altechna R&D. S-waveplate - linear to radial polarization converter. operation manual. <http://www.altechna.com/download/wop/Operation-Manual-130701.pdf>, (2013).
- [20] V. Rico-Botero. Master in optics vmricob. <https://sites.google.com/a/correounivalle.edu.co/master-in-optics-vmricob/home/simulations>, (2015).
- [21] Izcoatl Saucedo-Orozco, Rafael Espinosa-Luna, and Qiwen Zhan. Angularly-resolved variable wave-retarder using light scattering from a thin metallic cylinder. *Optics Communications*, **352**:135 – 139, (2015).
- [22] C. See, M. Somekh, and R. Holmes. Scanning optical microellipsometer for pure surface profiling. *Appl. Opt.*, **35**(34):6663–6668, (1996).
- [23] Thorlabs. Shearing interferometers. https://www.thorlabs.com/newgrouppage9.cfm?objectgroup_id=2970&pn=SI254, (2016).
-

-
- [24] Jiming Wang, Weibin Chen, and Qiwen Zhan. Engineering of high purity ultra-long optical needle field through reversing the electric dipole array radiation. *Opt. Express*, 18(21):21965–21972, (2010).
- [25] Gregory J. Ward. Measuring and modeling anisotropic reflection. *SIG-GRAPH-92 proceedings*, pages 265–272, (1992).
- [26] R. Webb. Confocal microscopes. *Opt. Phot. News*, 2:8–12, (1991).
- [27] Sang-Heon Ye, Soo Hyun Kim, Yoon Keun Kwak, Hyun Mo Cho, Yong Jai Cho, and Won Chegal. Angle-resolved annular data acquisition method for microellipsometry. *Opt. Express*, **15**(26):18056–18065, (2007).
- [28] Q. Zhan. Cylindrical vector beams: from mathematical concepts to applications. *Adv. Opt. Photon.*, 1:1–57, (2009).
- [29] Q. Zhan. *Vectorial Optical Fields: Fundamentals and Applications*. World Scientific Publishing Company, (2013).
-